Modeling oceanic nitrate and nitrite concentrations and isotopes using a 3D inverse N cycle model

Taylor S. Martin[1], François Primeau[2], Karen L. Casciotti[1*]

[1]Stanford University, Department of Earth System Science
[2]University of California, Irvine, Department of Earth System Science

[*]Corresponding author: kcasciotti@stanford.edu; 650-721-5545

Abstract. Nitrite (NO_2^-) is a key intermediate in the marine nitrogen (N) cycle and a substrate in nitrification, which produces nitrate (NO_3^-), as well as water column N loss processes, denitrification and anammox. In models of the marine N cycle, NO_2^- is often not considered as a separate state variable, since NO_3^- occurs in much higher concentrations in the ocean. In oxygen deficient zones (ODZs), however, NO_2^- represents a substantial fraction of the bioavailable N, and modeling its production and consumption is important to understanding the N cycle processes occurring there, especially those where bioavailable N is lost from or retained within the water column. Improving N cycle models by including NO_2^- is important in order to better quantify N cycling rates in ODZs, particularly N loss rates. Here we present the expansion of a global 3D inverse N cycle model to include NO_2^- as a reactive intermediate as well as the processes that produce and consume NO_2^- in marine ODZs. NO_2^- accumulation in ODZs is accurately represented by the model involving NO_3^- reduction, NO_2^- reduction, NO_2^- oxidation, and anammox. We model both ^{14}N and ^{15}N and use a compilation of oceanographic measurements of NO_3^- and NO_2^- concentrations and isotopes to place a better constraint on the N cycle processes occurring. The model is optimized using a range of isotope effects for denitrification and NO_2^- oxidation, and we find that the larger (more negative) inverse isotope effects for NO_2^- oxidation along with relatively high rates of NO_2^- oxidation give a better simulation of NO_3^- and NO_2^- concentrations and isotopes in marine ODZs.

1 Introduction

Nitrogen (N) is an important nutrient to consider when assessing the biogeochemical cycling in the ocean. The N cycle is intrinsically tied to the carbon (C) cycle, whereby N can be the limiting nutrient for primary production and carbon dioxide uptake (Moore et al., 2004; Codispoti, 1989). Understanding the distribution and speciation of bioavailable N in the ocean allows us to make inferences about the effects on other nutrient cycles and potential roles that N may play in a regime of climate change (Gruber, 2008).

There are several chemical species in which N can be found in the ocean. The largest pool of bioavailable N is nitrate (NO_3^-), a dissolved inorganic species, which can be taken up by microbes for use in assimilatory or dissimilatory processes. Another dissolved inorganic species, nitrite (NO_2^-), accumulates in much lower concentrations but is a key intermediate in many N cycling processes. Models of the marine N cycle often include NO_3^- and NO_2^- together as a single dissolved inorganic N (DIN) pool, or exclude NO_2^- entirely (DeVries et al., 2013; Deutsch et al., 2007; Brandes and Devol, 2002). However, NO_2^- does accumulate significantly in oxygen deficient zones (ODZs) in features known as secondary NO_2^- maxima, and it is an intermediate or substrate in many important N cycle processes occurring there.

ODZs are hotspots for marine N loss (Codispoti et al., 2001; Deutsch et al., 2007), which is driven by processes that result in conversion of bioavailable DIN to dinitrogen gas (N_2). The two main water column N loss processes, denitrification and anammox, use NO_2^- as a substrate. Denitrification involves the stepwise reduction of NO_3^- to NO_2^- and then to gaseous nitric oxide (NO), nitrous oxide (N_2O), and N_2. Anammox consists of the anaerobic oxidation of ammonium (NH_4^+) to N_2 using NO_2^- as the electron acceptor. NO_2^- is also oxidized to NO_3^- during anammox, representing an alternative fate for NO_2^- in ODZs. Indeed, NO_2^- oxidation appears to be prevalent in ODZs, with more NO_2^- oxidation occurring than can be explained by anammox alone (Gaye et al., 2013; Peters et al., 2016; Peters et al., 2018; Babbin et al., 2017; Buchwald et al., 2015; Casciotti et al., 2013; Martin and Casciotti, 2017). NO_2^- oxidation results in the regeneration of NO_3^- that would otherwise be converted to N_2 and lost from the system. The close coupling between NO_3^- reduction to NO_2^- and NO_2^- oxidation back to NO_3^- represents a control valve on the marine N budget (Penn et al., 2016; Bristow et al., 2016). Where NO_2^- oxidation can outcompete NO_2^- reduction via denitrification and anammox, bioavailable N is retained. Water column N losses only occur where NO_2^- oxidation rates are limited by oxygen availability. Thus, understanding the NO_2^- dynamics in ODZ waters is critical to assess the N loss occurring there.

The observed NO_3^- and NO_2^- concentrations alone do not allow us to fully characterize the N cycling processes occurring in a given region. Stable isotope measurements of NO_3^- and NO_2^- provide additional insight and constraints on marine N cycle processes. There are two stable isotopes of N, ^{14}N and ^{15}N. The isotopic ratios for a given N species, usually expressed in delta notation as $\delta^{15}N$ (‰) = ($^{15}N/^{14}N_{sample} \div {}^{15}N/^{14}N_{standard}$ -1)$\times$1000, is an integrated measure of the processes that have produced and consumed that N species. Each process imparts a unique isotope effect ($\varepsilon = {}^{14}k/^{15}k$ -1 $\times$ 1000, where ^{14}k and ^{15}k are the first order rate constants for the ^{14}N and ^{15}N containing molecules, respectively) that impacts the isotopic composition of the substrate and the product (Mariotti et al., 1980). In particular, NO_2^- cycling processes have distinct isotope effects for NO_2^- reduction, which occurs with normal isotopic fractionation (Bryan et al., 1983; Martin and Casciotti, 2016; Brunner et al., 2013) and NO_2^- oxidation, which occurs with an unusual inverse kinetic isotope effect (Casciotti, 2009; Buchwald and Casciotti, 2010; Brunner et al., 2013). Thus, the isotopes of NO_2^- are very sensitive to the relative importance of NO_2^- oxidation and NO_2^- reduction in NO_2^- consumption (Casciotti, 2009; Casciotti et al., 2013).

Models of the marine N cycle have employed isotopes and isotope effects in conjunction with N concentrations to elucidate N cycle processes (Brandes and Devol, 2002; Sigman et al., 2009; Somes et al., 2010; DeVries et al., 2013; Casciotti et al., 2013; Buchwald et al., 2015; Peters et al., 2016). A model can either assume a set of processes and infer the underlying isotope effects, or assume isotope effects and infer a set of processes. These isotope models are highly dependent on the chosen isotope effects used for given processes. Though there are estimates of isotope effects for processes based on both environmental measurements and laboratory studies, there is not always agreement between them. For example, laboratory cultures of NO_2^- oxidizers indicate an N isotope effect of $^{15}\varepsilon = -10$ to $-20‰$ (Casciotti, 2009; Buchwald and Casciotti, 2010), while measured concentrations and isotopes of NO_3^- and NO_2^- in ODZs indicate that isotope effects closer to $-30‰$ are more consistent with the observations (Buchwald et al., 2015; Casciotti et al., 2013; Peters et al., 2016).

Here we present an expansion of an existing global ocean 3D inverse isotope-resolving N cycling model (DeVries et al., 2013) to investigate the isotopic constraints on N cycling in ODZs and the impact of these regions on global ocean N isotope patterns. An important step was to include NO_2^- and its isotopes as tracers. The addition of NO_2^- allows us to include additional internal N cycling processes, as well as a more nuanced and realistic version of the processes occurring in ODZs. We used a database of NO_3^- and NO_2^- observations in order to assess the performance of the model as well as optimize the model N cycle parameters for which we do not have good prior estimates. In the model we employ a variety of isotope effect estimates for three important ODZ processes—NO_3^- reduction, NO_2^- reduction, and NO_2^- oxidation—to discern what isotope effect estimates result in the best fit to the observations.

2 Methods

2.1 Inverse nitrogen cycle model overview

The model used here is a steady-state inverse model that solves for the concentration and $\delta^{15}N$ of NO_3^-, NO_2^-, particulate organic N (PON), and dissolved organic N (DON) using a set of linear equations. Because the model assumes that the system is in steady state, it is not able to capture time-dependent properties of the system such as seasonality and anthropogenic change. However, on inter-annual timescales the N cycle is thought to be approximately in balance (Gruber, 2004; Bianchi et al., 2012). The residence time of N in the ocean, which is thought to be on the order of 2000-3000 years (Gruber, 2008), is sufficiently long to preclude any detectable changes in the global N inventory to date on timescales commensurate with the global overturning circulation. An important advantage of the steady-state assumption for our linear model is that it is possible to find solutions by direct matrix inversion without the need for a spin-up period as required by forward models. The solution to the system provides ^{14}N and ^{15}N concentrations of the N species of interest at every grid point in the model system. Working with a linear system imposes some restrictions on how complicated the rate equations can be, but there are improvements in model performance and ease of use, allowing us to test hypotheses about the processes that govern the marine N cycle and budget, particularly those occurring in and around oceanic oxygen deficient zones. We aimed to produce a realistic N cycle

model that represented ODZ processes accurately while limiting the number of free parameters. The description below outlines the dependencies and simplifications employed in this version of the model.

The model's uncertain biological parameters were determined through an optimization process that minimizes the difference between the modeled and observed NO_3^- and NO_2^- concentration and isotope data. Computational time limits the number of parameters that we were able to optimize. We therefore focused our investigation on parameters that are poorly constrained by literature values and to which the model solution is most sensitive. In order to determine the parameters for optimization, a sensitivity analysis was performed on each parameter, varying them individually by ±10% and computing the change in the modeled ^{14}N and ^{15}N. Those parameters that resulted in modeled ^{14}N and ^{15}N variability of >5% were chosen for optimization in the model. The sensitivity analysis and the optimal values of the parameters contribute to an improved understanding of the cycling of nitrogen in the ocean in general and in the ODZs in particular. The optimization process is discussed in further detail in Section 2.6.

The sensitivity analysis revealed that the modeled distribution of ^{15}N was very sensitive to isotope effects, parameters that control the relative rates of ^{15}N and ^{14}N in chemical and biological processes. There are literature estimates for each of the isotope effects of interest in this work, although there is often a discrepancy between isotope effects estimated in laboratory studies and those expressed in oceanographic measurements (Kritee et al., 2012; Casciotti et al., 2013; Bourbonnais et al., 2015; Martin and Casciotti, 2017; Fuchsman et al., 2017; Marconi et al., 2017; Peters et al., 2018b). Rather than optimizing the isotope effect values, we have chosen to use multiple cases with different combinations of previously estimated isotope effects in order to assess which values best fit the observations.

In addition to the optimized parameters and isotope effects, there were some non-sensitive parameters that were fixed prior to the optimization and whose values were chosen using literature estimates (Table 1). Some N cycle processes are also dependent on prescribed input fields that are not explicitly modeled, such as temperature, phosphate, oxygen, and net primary production. These external input fields will be discussed in detail in the relevant sections for each N cycle process.

2.2 Model grid and transport

The model uses a uniform 2°x2° grid with 24 depth levels. The thickness of each model layer increases with depth, from 36 m at the top of the water column to 633 m near the bottom. Bottom topography was determined using 2-minute gridded bathymetry (ETOPO2v2) that was then interpolated to the model grid. Our linear N cycle model relies on the transport of dissolved N species (NO_3^-, NO_2^-, and DON) in the ocean. For this we use the annual averaged circulation as captured by a tracer transport operator that governs the rate of transport of dissolved N species (NO_3^-, NO_2^-, and DON) between boxes. The original version of the tracer data-assimilation procedure used to generate the transport operator for dissolved species (T_f) is described by DeVries and Primeau (2011), and the higher resolution version used here is described by DeVries et al. (2013).

2.3 N cycle

In the N cycling portion of the model, we track four different N species (Figure 1). There are two organic N (ON) pools: dissolved (DON) and particulate (PON). There are also two dissolved inorganic N (DIN) pools: NO_3^- and NO_2^-. We did not explicitly model ammonium (NH_4^+) because it typically occurs in low concentrations throughout the ocean, and scarcity of data (especially ^{15}N data) would make model validation difficult. Though NH_4^+ has been observed to accumulate to micromolar concentrations in some ODZs (Bristow et al., 2016; Hu et al., 2016), this occurs largely in shallow, coastal shelf regions that are not resolved by the model.

Because we used the concentrations of both ^{14}N and ^{15}N of each N species to constrain the rate parameters, two sets of governing equations were employed: one that depends on ^{14}N and another that depends on [15]N. Generally, the rate for ^{15}N processes was dependent on the rate of ^{14}N processes and an isotopic fractionation factor (α) that is specific to each process and substrate. By solving for steady-state solutions to both ^{14}N and ^{15}N concentrations, we were able to model global distributions of [NO_3^-], [NO_2^-], and their corresponding $\delta^{15}N$ values.

2.3.1 N cycle parameterization

We will first address the ^{14}N equations and the general format of the N cycle in the model. Each equation is then broken down into its component parts for further explanation of the biological processes and their parameterization. The ^{15}N equations and isotope implementation will be discussed in a later section.

The governing equations for the ^{14}N-containing DIN (NO_3^- and NO_2^-) and organic N (DON and PON) state variables can be written as follows:

1. $\left[\frac{\partial}{\partial t} + T_f\right] {}^{14}NO_3^- = J_{14}^{dep} - J_{14}^{assim,NO3} - J_{14}^{NAR} + J_{14}^{NXR} + 0.3J_{14}^{AMX} - J_{14}^{sed}$

2. $\left[\frac{\partial}{\partial t} + T_f\right] {}^{14}NO_2^- = J_{14}^{AMO} - J_{14}^{assim,NO2} + J_{14}^{NAR} - J_{14}^{NXR} - J_{14}^{NIR} - 1.3J_{14}^{AMX}$

3. $\left[\frac{\partial}{\partial t} + T_f\right] DO^{14}N = \sigma(J_{14}^{fix} + J_{14}^{assim,WOA}) + J_{14}^{sol} - J_{14}^{remin}$

4. $\left[\frac{\partial}{\partial t} + T_p\right] PO^{14}N = (1 - \sigma)(J_{14}^{fix} + J_{14}^{assim,WOA}) - J_{14}^{sol}$

The model is designed to represent a steady state, thus the $\frac{\partial}{\partial t}$ term is 0. The J terms represent the source and sink processes for each state variable, expressed in units of mmol/m³/yr and will be described in more detail below. Briefly, J_{14}^{dep} is the spatially-variable deposition of NO_3^- from the atmosphere to the sea surface. In the DIN model equations, $J_{14}^{assim,NO3}$ and $J_{14}^{assim,NO2}$ represent the assimilation of NO_3^- and NO_2^-, respectively, by phytoplankton in the upper two box levels. This assimilated NO_3^-

produces DON and PON, with proportions set by a spatially-variable term, σ. Assimilation in the DON and PON equations is represented by $J_{14}^{assim,WOA}$ and is dependent on 2013 World Ocean Atlas (WOA) [NO_3^-] interpolated to the model grid. N_2 fixation (J_{14}^{fix}) is split between DON and PON with the same σ term. NO_3^- reduction (J_{14}^{NAR}), NO_2^- reduction (J_{14}^{NIR}), NO_2^- oxidation (J_{14}^{NXR}), and anammox (J_{14}^{AMX}) act on the NO_3^- and NO_2^- pools. J_{14}^{sed} represents the removal of NO_3^- via benthic

5   denitrification. J_{14}^{sol} represents the dissolution of PON into DON. J_{14}^{remin} represents the degradation of DON, which feeds into ammonia oxidation (J_{14}^{AMO}) and J_{14}^{AMX} as described below.

Through the use of these J terms, the governing equations are all linear with respect to the state variables. However, in order to introduce dependence of rates on the concentrations of multiple state variables, for example allowing heterotrophic NO_3^-

10   reduction to be dependent on organic N as well as NO_3^-, we run the organic N equations first and the DIN equations second. When [DON] is found in the [DIN] governing equations, that [DON] value has already been determined for each grid box from the organic N model. When [NO_3^-] is found in the DON governing equations, it is drawn from 2013 World Ocean Atlas annual data interpolated to the model grid.

2.3.2 N source processes

15   Atmospheric deposition and N_2 fixation are the only sources of new bioavailable N in the model. These are the two largest sources of N to the ocean (Gruber and Galloway, 2008). We do not consider the third largest source of N, riverine fluxes, in the model due to lack of coastal resolution and the expectation that much of the river-derived N is denitrified in the shelf sediments (Nixon et al., 1996; Seitzinger and Giblin, 1996). Representing these processes may be possible in a future version of the model, but is beyond the scope of the current model, given its coarse resolution near the coasts.

Atmospheric deposition

N deposition is assumed to only occur in the top box of the model, and we assume that most of the N deposited is as NO_3^-, and that the other species would be rapidly oxidized to NO_3^- in the oxic surface waters.

25   5. $J_{14}^{dep} = r_{14}^{dep} S^{dep}$

To calculate J_{14}^{dep}, the atmospheric deposition rate of ^{14}N, we use modeled total inorganic N deposition for 1993, S^{dep} (Galloway   et   al.,   2004;   Dentener   et   al.,   2006;   data   available   online   at https://daac.ornl.gov/CLIMATE/guides/global_N_deposition_maps.html), which was interpolated to our model grid. This

30   term, S^{dep}, is then multiplied by a prescribed fractional abundance of ^{14}N in the deposited N (r_{14}^{dep}), which is calculated from the isotopic composition of deposited N ($\delta^{15}N_{dep}$, -4‰; Equation 6), to yield the deposition of ^{14}N to the sea surface in each

box (J_{14}^{dep}). To calculate r_{14}^{dep} from $\delta^{15}N_{dep}$, we first calculate r_{15}^{dep} using r_{15}^{air}, a standard with a value of 0.003676 (Equation 6; Mariotti, 1983).

$$6. \quad r_{15}^{dep} = \left(\frac{\delta^{15}N_{dep}}{1000} + 1\right) \times r_{15}^{air}$$

Then, assuming that $[^{14}N] \sim [^{14}N] + [^{15}N]$, we calculate r_{14}^{dep} as $(1 - r_{15}^{dep})$. The units of S^{dep} are given in mg N/m²/yr, which we convert to mmol NO_3^-/m³/yr via dimensional analysis and by dividing by the depth of the surface box. This source term of N to the model is independent of the modeled N terms.

10 **N₂ fixation**

N₂ fixation is the other source of new N to the model, and is assumed to only occur in the top box of the model. It is parameterized similarly to N₂ fixation in the model of DeVries et al. (2013), with partial inhibition by NO_3^- (Holl and Montoya, 2005) and dependence on iron (Fe) and phosphate (PO_4^{3-}) availability (Monteiro et al., 2011).

15 $$7. \quad J_{14}^{fix} = r_{14}^{fix} F_0 \, e^{-NO_{3,obs}/\lambda} \, e^{\frac{T_{obs} - T_{max}}{T_0}} \frac{Fe}{Fe + K_{Fe}} \frac{PO_4}{PO_4 + K_P}$$

F_0 is the maximum rate of N₂ fixation (1.5 mmol/m³/yr; Table 1) and is calculated from the estimated areal rate of N₂ fixation in the western tropical Atlantic (Capone et al., 2005) divided by the depth of the top model box. $NO_{3,obs}$ is the 2013 World Ocean Atlas annually averaged surface NO_3^- interpolated to the model grid (Garcia et al., 2014). λ is an inhibition constant for

20 N₂ fixation in the presence of NO_3^- (Table 1).

The temperature (T) terms scale the rate of N₂ fixation based on the observed temperature (T_{obs}), maximum observed sea surface temperature (T_{max}), and the minimum preferred growth temperature for *Trichodesmium* (T_0; Capone et al., 2005). The temperature data were taken from 2013 World Ocean Atlas annually averaged temperature interpolated to the model grid

25 (Locarnini et al., 2013). We recognize that this will likely provide a conservative estimate of N₂ fixation, given the growing recognition of N₂ fixation outside of the tropical and subtropical ocean by organisms other than *Trichodesmium* (Shiozaki et al., 2017; Harding et al., 2018; Landolfi et al., 2018).

Fe is the modeled deposition of soluble Fe interpolated to the model grid (mmol Fe/m²/yr; Chien et al., 2016) divided by the

30 depth of the top model grid box to give units of mmol Fe/m³/yr. Fe and PO_4^{3-} are assumed to limit N₂ fixation at low concentrations via Michaelis-Menten kinetics. K_{Fe} and K_P are their respective half-saturation constants. Additionally, there is a term that allows us to set the isotopic ratio of newly fixed N, r_{14}^{fix}, which is the fractional abundance of ^{14}N in newly fixed N

and is calculated as in Equation 6 from $\delta^{15}N_{fix}$ (-1‰; Table 1). All of the N_2 fixation parameters are fixed rather than optimized (Table 1). Due to the use of non-optimized parameters and an input NO_3^- field rather than modeled NO_3^-, N_2 fixation serves as an independent check that our modeled N cycle produces reasonable N concentrations and overall N loss rates. However, N_2 fixation is not explicitly modeled here and is instead taken as a fixed, though spatially variable, input field (Figure S1). The global rate of N_2 fixation produced by this parameterization is 131 Tg N/yr, which is in line with several current estimates (Table S1).

In the model, N_2 fixation and NO_3^- assimilation (Section 2.3.3) are assumed to be the two processes that create exportable organic N. A fraction, σ, of this organic N is portioned into DON rather than PON (Equations 3-4). In order to create spatial variability in this constant, we assumed (1-σ), the fraction of assimilated N partitioned to PON, is equal to the particle export (P_e) ratio. This P_e ratio is the ratio of particle export to primary production, and is equivalent to the fraction of organic N that is exported from the euphotic zone as particulate matter rather than recycled or solubilized into DON. The P_e ratio is calculated for each model grid square from the mixed layer temperature (T_{ml}) and net primary production (NPP) as described by Dunne et al. (2005):

$$8. \quad P_e = \phi T_{ml} + 0.582 \log(NPP) + 0.419$$

The constant ϕ has a value of -0.0101 $°C^{-1}$ as determined by Dunne et al. (2005). Net primary production estimates in units of mmol carbon/m^2/yr were taken from a satellite-derived productivity model (Westberry et al., 2008), annually averaged, and interpolated onto the model grid. T_{ml} is calculated from the 2013 World Ocean Atlas annual average (Locarnini et al., 2013), which has been interpolated to the model grid. The temperature of the top two model boxes were averaged to give T_{ml}. As temperature increases, the P_e ratio decreases and less PON is exported, resulting in more DON recycling in the surface with several possible explanatory mechanisms discussed in greater detail by Dunne et al. (2005). As net primary production increases, the P_e ratio increases and more PON is exported; net primary production explains 74% of the observed variance in particle export (Dunne et al., 2005).

2.3.3 Internal N cycling processes

Assimilation of nitrate and nitrite

Assimilation accounts for the uptake of DIN and its incorporation into organic matter in the shallowest two layers of the global model. Since assimilation affects both the organic and inorganic N pools, we must account for it in both sets of model runs. We will first address assimilation in the organic N model (Equations 9 and 10).

$$9. \quad J_{14}^{assim,WOA} = {}^{14}k_{assim}[NO_3^-]_{obs}$$

10. $^{14}k_{assim} = \dfrac{NPP}{r_{C:N}[NO_3^-]_{obs}}$

Since the organic N model is run first and the assimilation rates are dependent on DIN concentrations, assumptions must be made about the DIN field in order to account for assimilation prior to the DIN model runs. Here we used observed [NO$_3^-$] from the 2013 World Ocean Atlas annual product interpolated to the model grid [NO$_3^-$]$_{obs}$ (Garcia et al., 2014) to calculate the assimilation rates for DON and PON production ($J_{14}^{assim,WOA}$). For this assumption to be valid, our modeled surface [NO$_3^-$] must be close to the observed values, which we will test in Section 3.1. The rate constant for assimilation, $^{14}k_{assim}$, varies spatially and is determined using observations of surface [NO$_3^-$] and satellite derived net primary production estimates (NPP; Westberry et al., 2008). The rate constant is converted to N units using the ratio of carbon (C) to N in organic matter ($r_{C:N}$) which we assume to be 106:16 (Redfield et al., 1963). The value of the rate constant is only non-zero in the top two boxes of the model, where we assume primary production to be occurring. The same rate constant is used in both the organic N and DIN assimilation equations. We also assume from the perspective of organic N that only NO$_2^-$ is being assimilated, since NO$_2^-$ is present at relatively low concentrations in the surface ocean, and it may be characterized as recycled production. Assimilated N is partitioned between PON and DON using the P_e ratio as previously described and shown in Equations 3 and 4.

The setup for assimilation in the DIN model (Equations 11 and 12) is similar, but can use modeled [NO$_3^-$] and [NO$_2^-$] rather than the World Ocean Atlas values. In order to appropriately reflect surface NO$_3^-$ and NO$_2^-$ concentrations, both NO$_3^-$ and NO$_2^-$ are assimilated. $^{14}k_{assim}$ is calculated as described above and is assumed to be the same for both NO$_3^-$ and NO$_2^-$. We justify using only [NO$_3^-$] to parameterize $^{14}k_{assim}$ because NO$_3^-$ generally makes up the bulk of DIN available for assimilation at the surface, but this assumption will be discussed in more detail below.

11. $J_{14}^{assim,NO3} = {}^{14}k_{assim}[^{14}NO_3^-]$

12. $J_{14}^{assim,NO2} = {}^{14}k_{assim}[^{14}NO_2^-]$

Solubilization

Solubilization is the transformation of PON to DON, and is dependent only on [PON] and a solubilization rate constant ($^{14}k_{sol}$), which is optimized (Table 2).

13. $J_{14}^{sol} = {}^{14}k_{sol}[PO^{14}N]$

The solubilization of PON, together with the particle transport operator (T_p), produces a particle flux attenuation curve similar to a Martin curve with exponent b = -0.858 (Table 1) (Martin et al., 1987). While in the real world, the length scale for particle flux attenuation is somewhat longer in ODZs compared to oxygenated portions of the water column, and also varies regionally

(Berelson et al., 2002; Buesseler et al., 2008; Buesseler and Boyd, 2009), our model uses a spatially-invariant $^{14}k_{sol}$. A spatially variable $^{14}k_{sol}$ that accounts for lower apparent values in ODZs is a refinement that could be introduced in future model versions.

Remineralization

5 Remineralization, or ammonification, is the release of DON into the DIN pool. This is determined using the concentration of DON and a remineralization rate constant ($^{14}k_{remin}$), which is optimized (Table 2).

$$14.\ J_{14}^{remin} = {}^{14}k_{remin}\left[DO^{14}N\right]$$

10 The removal of this remineralized DON, since it does not accumulate as NH_4^+, is either through ammonia oxidation (AMO) or anammox (AMX), depending on $[O_2]$ as described below and in Section 2.3.4. We use the same remineralization rate constant regardless of the utilized electron acceptor (e.g. O_2, NO_3^-). Since particle flux attenuation is observed to be somewhat weaker in oxygen deficient zones compared with oxygenated water (Van Mooy et al., 2002), this may slightly overestimate the rates of heterotrophic remineralization occurring in ODZs.

Ammonia oxidation

Ammonia oxidation (AMO) uses ammonia (NH_3) as a substrate. Since we do not include NH_3 or NH_4^+ in the model system, we treat remineralized DON as the substrate for AMO. In order to maintain consistency between the organic N and DIN model runs, remineralized DON is routed either to AMO or AMX (lost from the system) based on the O_2 dependencies of AMO and
20 AMX. Rather than using a strict O_2 cutoff for AMO, it is limited by O_2 using Michaelis-Menten kinetics. The half-saturation constant for O_2, K_m^{AMO} (Table 1), sets the O_2 concentration at which AMO reaches half of its maximal value.

$$15.\ J_{14}^{AMO} = (1 - \eta_{AMX})J_{14}^{rem} + \eta_{AMX}\frac{[O_2]}{[O_2] + K_m^{AMO}}\,J_{14}^{remin}$$

25 Recent studies have shown that AMO and NO_2^- oxidation (NXR), both O_2-requiring processes, have very low O_2 half saturation constants and can occur down to nM levels of $[O_2]$ (Peng et al., 2015; Bristow et al., 2016). In contrast, O_2-inhibited processes such as AMX are only allowed to occur at O_2 concentrations below a given threshold. The handling of O_2 thresholds for anaerobic processes is discussed in more detail below (Section 2.3.4), though we describe it briefly here due to the interplay between AMO and AMX in the model. Briefly, the O_2 dependence of AMX is represented by the parameter η_{AMX}, which has
30 a value between 0 and 1 for a given grid box depending on the average number of months in a year its 2013 World Ocean Atlas $[O_2]$ falls below the $[O_2]$ threshold for anammox (O_2^{AMX}, Table 1). If, for example, $[O_2]$ in a given grid box is always above the threshold for AMX, $\eta_{AMX} = 0$ and all of the remineralized DON (represented by J_{14}^{rem}) will be oxidized via AMO. If $[O_2]$ is less than O_2^{AMX}, η_{AMX} will be non-zero and a smaller fraction of the remineralized DON will be oxidized via AMO.

The fraction ultimately oxidized by AMO is thus determined by the Michaelis-Menten parameterization of AMO, as well as the O_2 threshold for anammox.

Nitrite oxidation

5   The rates of NO_2^- oxidation (NXR) are dependent on the availability of NO_2^- as well as O_2. Similar to AMO, we parameterize O_2 dependence using Michaelis-Menten kinetics and a fixed half-saturation constant for O_2 (K_m^{NXR}, Table 1). K_m^{NXR} was taken to be 0.8 μM O_2, based on kinetics experiments performed with natural populations of NO_2^- oxidizing bacteria (Bristow et al., 2016). Finally, we employ an optimized rate constant ($^{14}k_{NXR}$, Table 2) to fit the available data.

10   16. $J_{14}^{NXR} = {}^{14}k_{NXR}[{}^{14}NO_2^-]\frac{[O_2]}{[O_2]+K_m^{NXR}}$

2.3.4 N sink processes

Nitrate and nitrite reduction

NO_3^- reduction (NAR) and NO_2^- reduction (NIR) are two processes within the stepwise reductive pathway of canonical denitrification. The end result of denitrification is the conversion of DIN to N_2 gas, rendering it bioavailable to only a restricted

15   set of marine organisms. Although there are intermediate gaseous products between NO_2^- and N_2, we treat NIR as the rate-limiting step in the denitrification pathway, where DIN is removed from the system.

For both NAR and NIR, we introduce a dependency on two state variables, their respective N substrates, and organic matter availability. Where NAR and NIR occur heterotrophically, they consume organic matter in addition to their main N

20   substrates/electron receptors. When NAR occurs chemoautotrophically, it would be dependent primarily on the presence of NO_3^- and an electron donor, such as hydrogen sulfide (Lavik et al., 2009). Since we do not model the production of reduced sulfur species in our model, our estimates of denitrification would not explicitly include the effects of this process. However, chemolithotrophic denitrification could be tacitly accounted for in the optimization process, since the rate constants that control the rates of NAR and NIR are optimized in order to best fit the observations, and the isotope effect for chemolithotrophic

25   denitrification is thought to be similar to that of heterotrophic denitrification (Frey et al., 2014). In order to maintain levels of heterotrohpic NAR and NIR that are bounded both by the available NO_3^- or NO_2^- and the available organic matter in a linear model, it was necessary to run organic N and DIN equations separately, since it is not possible to include dependencies on two state variables (e.g. DON and NO_3^-) in the linear system. Both NAR and NIR are dependent on the remineralization rate (J_{14}^{remin}) that is calculated in the organic N model run. In model boxes where NAR and NIR are occurring, some of the

30   remineralization is carried out with electron acceptors other than O_2. For simplicity, we assume that J_{14}^{remin} does not depend on the choice of electron acceptor.

17. $J_{14}^{NAR} = \eta_{NAR} \, {}^{14}k_{NAR} [{}^{14}NO_3^-] J_{14}^{remin}$

18. $J_{14}^{NIR} = \eta_{NIR} \, {}^{14}k_{NIR} [{}^{14}NO_2^-] J_{14}^{remin}$

The rate coefficients for NAR (${}^{14}k_{NAR}$) and NIR (${}^{14}k_{NIR}$) are optimized rather than fixed (Table 2). Further, the dependence of J_{14}^{NAR} and J_{14}^{NIR} on J_{14}^{remin} means that k_{NAR} and k_{NIR} are not first order rate constants and have different units than k_{PON}, k_{DON}, and k_{NXR} (Table 2).

The inhibition of NAR and NIR by O_2, like AMX, is parameterized by a parameter η, which inhibits these processes when $[O_2]$ is above their maximum threshold. Originally, we treated this term as a binary operator where it would be 0 if the empirically-corrected 2013 World Ocean Atlas annually averaged $[O_2]$ is above the threshold for the process and 1 if $[O_2]$ is below the threshold. On further refinement, we wanted to account for the possibility of seasonal shifts in $[O_2]$ in ODZs. Thus, for each month, we assigned a value of 0 or 1 to each model grid box. These values were then averaged over the 12 months of the year to give a sliding value of η between 0 and 1 for each grid box. The O_2 thresholds used to calculate η_{NAR} and η_{NIR} were fixed (7 μM and 5 μM, respectively; Table 1). Since we do not explicitly model O_2, $[O_2]$ was predetermined using the 2013 World Ocean Atlas monthly O_2 climatology (Garcia et al., 2014) interpolated to the model grid. We also applied an empirical correction that improves the fit of World Ocean Atlas $[O_2]$ data to observed suboxic measurements (Bianchi et al., 2012).

Anammox

Anammox (AMX) catalyzes the production of N_2 from NH_4^+ and NO_2^-. Since we do not use NH_4^+ as a variable in our N cycling equations, we substituted remineralized DON (J_{14}^{remin}) as a proxy for NH_4^+ availability. As described above in Section 2.3.3, remineralized DON is routed through either AMO or AMX depending on $[O_2]$ and the O_2 dependencies of AMO and AMX.

19. $J_{14}^{AMX} = \eta_{AMX} \left(1 - \dfrac{[O_2]}{[O_2] + K_m^{AMO}}\right) J_{14}^{remin}$

The O_2 threshold used to calculate η_{AMX} from monthly O_2 climatology is fixed (10 μM; Table 1). In order to maintain mass balance on remineralized DON, we do not include dependence on $[NO_2^-]$ in Equation 19, although J_{14}^{AMX} removes NO_2^- (Equation 2). This parameterization inherently assumes that AMX is limited primarily by $[NH_4^+]$ supply and not $[NO_2]$, which may not always be correct (Bristow et al., 2016). Anammox also produces 0.3 moles of NO_3^- via associated NXR for every 1 mole of N_2 gas produced (Strous et al., 1999). For this reason, anammox appears in the state equation for NO_3^- (Equation 1).

Sedimentary denitrification

Sedimentary (or benthic) denitrification (J_{14}^{sed}) is an important loss term for N in the marine environment, and in order to encapsulate it within the model grid we assume that it is occurring within the bottom depth box for any particular model water column. The parameterization for sedimentary denitrification is based on a transfer function described by Bohlen et al. (2012). The original transfer function was dependent on bottom water [O_2], bottom water [NO_3^-], and the rain rate of particulate organic carbon (RRPOC). Here, RRPOC was calculated via a Martin curve (Martin et al., 1987) using the P_e ratio, net primary production (NPP), depth (z), euphotic zone depth (z_{eu}), and a Martin curve exponent (b):

$$20.\quad RRPOC = NPP * P_e * \left(\frac{z}{z_{eu}}\right)^b$$

Net primary production is derived from the productivity modeling of Westberry et al. (2008) as described in Section 2.3.2. The P_e ratio is calculated as previously described in Section 2.3.2. The depth for any given model box is assumed to be the depth at the bottom of the box. The euphotic zone depth is the bottom depth of the 2nd box (73 m), since all production is assumed to be occurring in the top two boxes. As described above, the Martin curve exponent, b, is a fixed value in our model ($b = -0.858$; Table 1), though this may result in underestimation of the particulate matter reaching the seafloor below ODZs (Van Mooy et al., 2002).

The transfer function for sedimentary denitrification was originally described using a non-linear dependence of the rate on ([O_2] – [NO_3^-]). In order for sedimentary denitrification to be properly implemented in our linear model, we broke the original non-linear relationship into three roughly linear segments to create a piecewise relationship between ([O_2] – [NO_3^-]) and sedimentary denitrification rate (Figure S2). We obtained three linear relationships between ([O_2] – [NO_3^-]) and sedimentary denitrification rate, each applicable across a given range of ([O_2] – [NO_3^-]) values. Due to the nature of our linear model, we needed to express the interval cutoff points that define the transition between the piecewise relationship segments in terms of O_2 rather than ([O_2] – [NO_3^-]). Therefore, a linear relationship between O_2 and ([O_2] – [NO_3^-]) was determined using the 2013 World Ocean Atlas annually averaged data (Garcia et al., 2014; Figure S3). The cutoff points were determined to be 75 μM O_2 and 175 μM O_2. The linear relationships were then rearranged in order to estimate sedimentary denitrification rate as a function of RRPOC, [O_2], and [NO_3^-]. These equations were then further broken down into a component that is dependent on [NO_3^-] and a component that is dependent on [O_2].

An additional term is introduced that reduces the sedimentary denitrification rate by 27% if the depth of the bottom model box is less than 1000 m. This term represents the potential for efflux of NH_4^+ into the water column from shallow, organic rich shelf sediments (Bohlen et al., 2012). This decreases overall sedimentary denitrification by approximately 6 Tg N/yr. This transfer function also assumes that all of the NH_4^+ efflux is immediately oxidized to NO_3^- and does not alter its isotopic

composition in bottom water. This is a conservative estimate of the effects of benthic N loss on water column NO_3^- isotopes, as several studies suggest that benthic N processes may contribute to water column nitrate ^{15}N-enrichment (Lehmann et al., 2007; Granger et al., 2011; Somes et al., 2015; Brown et al., 2015). However, our current model parameterization does not require enhanced fractionation during benthic N loss to fit deep ocean $\delta^{15}N_{NO3}$. Additionally, our spatial resolution does not
5   well represent regions where this effect might be significant on bottom water $\delta^{15}N_{NO3}$, such as the shallow shelves.

2.4 N isotope implementation

In our model, we are interested in using the isotopic composition of NO_3^- and NO_2^- to constrain the rates of N cycling and loss from the global ocean. As DON and PON are ultimate substrates for NO_2^- and NO_3^- production, it is essential to track the ^{15}N in the organic N pools as well. The matrix setup for ^{15}N is similar to that for the ^{14}N species, but the rates were changed as
10   follows:

$$21. \quad J_{15}^{process} = 1/\alpha_{process} \frac{[^{15}N_{substrate}]}{[^{14}N_{substrate}]} J_{14}^{process}$$

$J_{14}^{process}$ is the rate of each relevant ^{14}N process as described above, and $J_{15}^{process}$ is the rate of each ^{15}N process. $\alpha_{process}$ is the
15   fractionation factor for a given process, which is given by the ratio between the rate constants for ^{14}N and [15]N ($\alpha = {}^{14}k/{}^{15}k$). A fractionation factor greater than 1 indicates a normal isotope effect and a fractionation factor less than 1 indicates an inverse isotope effect. Several of these fractionation factors are well known, but others are more poorly constrained, especially when values are calculated from *in situ* concentration and isotope ratio measurements (Hu et al., 2016; Casciotti et al., 2013; Ryabenko et al., 2012). For this reason, we ran several model cases with different fractionation factors for NAR, NIR, and
20   NXR during the optimization process (Section 2.6, Table 3). The other fractionation factors were fixed (Table 1). In order to produce the ^{15}N concentrations of N species from our observations to constrain the model, we calculated ^{15}N/^{14}N from measured $\delta^{15}N$, and assumed that $[^{14}N] \sim [^{14}N] + [^{15}N]$, the measured concentration of each modeled N species.

This simple ^{15}N implementation was used with fixed fractionation factors for remineralization ($\alpha_{remin} = 1$), solubilization (α_{sol}
25   $= 1$), assimilation ($\alpha_{assim} = 1.004$), sedimentary denitrification ($\alpha_{sed} = 1$), and AMO ($\alpha_{AMO} = 1$) (Table 1). Isotope effects for NAR (ε_{NAR}), NIR (ε_{NIR}), and NXR (ε_{NXR}) were varied in different combinations during model optimization (Table 3). Distinct isotopic parameterizations were also required for atmospheric deposition, N_2 fixation and anammox, as described below.

Atmospheric deposition
30   For atmospheric deposition of N, we prescribe a constant $\delta^{15}N$ value of -4‰ (Table 1), which can be related to the fractional abundance of ^{14}N, previously described in Section 2.3.2 as r_{14}^{dep}, and the fractional abundance of [15]N (r_{15}^{dep}) in deposited N. We multiply r_{15}^{dep} by S^{dep}, the estimated rate of total N deposition, to obtain J_{15}^{dep}.

Nitrogen fixation

Similar to atmospheric deposition, newly fixed N has a constant prescribed $\delta^{15}N$ value (-1‰; Table 1). In Section 2.3.2 we described r_{14}^{fix}, the fractional abundance of ^{14}N in newly fixed N. Here we multiply the fractional abundance of ^{15}N, r_{15}^{fix}, by the other terms in the N_2 fixation equation (Equation 6) to obtain the rate of ^{15}N fixation.

Anammox

Anammox is the most complicated process to parameterize isotopically because it has three different N isotope effects associated with it. There is an isotope effect on both substrates that are converted to N_2 (NO_2^- and NH_4^+), as well as for the associated NO_2^- oxidation to NO_3^-. We assume that the fractionation factor for ammonium oxidation via AMX ($\alpha_{AMX,NH4}$) is 1, setting it to match the fractionation factor for AMO (α_{AMO}; Table 1), both with no expressed fractionation since NH_4^+ does not accumulate in the model. Since all remineralized DON must be routed either through AMO or AMX, this simplifies the mass balance and ensures that all remineralized ^{14}N and ^{15}N is accounted for. $^{15}NO_2^-$ is removed with the isotope effects of NO_2^- reduction ($\alpha_{AMX,NIR}$) and NO_2^- oxidation ($\alpha_{AMX,NXR}$), in the expected 1:0.3 proportion (Brunner et al., 2013).

2.5 Model inversion

Once our N cycle equations were set up as described above, we input them into MATLAB in block matrix form. The equations were of the general form $Ax = b$. All model ocean boxes (200,160 in total) are accounted for in the matrices. Matrix A (400,320 x 400,320) contained the rate constants and other parameters that are multiplied by the vector of state variables, x (400,320 x 1). Vector x contained the state variables (i.e. $[NO_3^-]$ and $[NO_2^-]$ or $[DON]$ and $[PON]$) to be solved for by the linear solver. Vector b (400,320 x 1) contained the rates that were independent of the state variables, such as N_2 fixation and N deposition. Let us consider, as an example, the DIN model setup. The top left corner of matrix A would contain rate constants for processes that produce and consume NO_3^- that are also dependent on $[NO_3^-]$. The top right corner of matrix A would contain rate constants for processes that produce and consume NO_3^- but are dependent on $[NO_2^-]$. The bottom left corner of matrix A would contain rate constants for processes that produce and consume NO_2^- but are dependent on $[NO_3^-]$. The bottom right corner of matrix A would contain rate constants that produce and consume NO_2^- and are also dependent on $[NO_2^-]$. The top half of vector x would be $[NO_3^-]$ for each model box, and the bottom half of vector x would be $[NO_2^-]$ for each model box. The top half of vector b would be independent processes that produce or consume $[NO_3^-]$, and the bottom half of vector b would be independent processes that produce or consume $[NO_2^-]$.

In MATLAB, we used METIS ordering, which is part of SuiteSparse (http://faculty.cse.tamu.edu/davis/suitesparse.html) to order our large, sparse matrix A. We then used the built-in function `umfpack` with METIS to factorize matrix A. The built-in matrix solver `mldivide` was then used with the factorized components of matrix A and matrix b to solve for x.

2.6 Parameter optimization

There are many parameters in the model that control the rates of the different N cycle processes (Tables 1-3). Some of these parameters are well constrained by literature values (Table 1). Others, such as the rate constants, were objects of our investigation and were optimized against available observations (Table 2). For our optimization, we compared model output using different parameter values to a database of NO_3^- and NO_2^- concentrations and isotopes. The database was originally compiled by Rafter et al. (in prep.) and has been expanded to include some additional unpublished data (Table S2). All of the database observations were binned and interpolated to the model grid. If multiple observations occurred within the same model grid box, the values were averaged and a standard deviation was calculated. The database was divided randomly into a training set, used for optimization, and a test set, used to assess model performance. The same number of grid points with observations was used in the training and test sets.

The optimization procedure used the MATLAB function `fminunc` to obtain values for the non-fixed parameters that minimized a cost function (Equation 22). In each iteration of the optimization, the model system was solved by running the ^{14}N-organic N model, ^{15}N-organic N model, ^{14}N-DIN model, and ^{15}N-DIN model. The modeled output $[NO_3^-]$, $[NO_2^-]$, $\delta^{15}N_{NO3}$, and $\delta^{15}N_{NO2}$ were compared to values from the database training set. Though DON and PON observations were not used to optimize the model, the open ocean and deep water NO_3^- values were useful in constraining the parameters that control PON solubilization and DON remineralization. The entire model was run using a set of initial parameter values (Table 2) and the optimization scheme continued to alter those starting parameters until a minimum in the cost function was attained. We optimized the logarithm of the parameter values rather than the original parameters themselves so the unconstrained optimization returned positive values. The transformed starting parameters and subsequent modified parameter sets were then fed back into the model equations as e^x, where x denotes the log-transformed parameter. The cost function in the optimization procedure is as follows:

$$22. \quad Cost = \frac{w_{NO3}}{n_{NO3}sd_{NO3}}\sum([NO_3^-]_{model} - [NO_3^-]_{training})^2 + \frac{w_{NO2}}{n_{NO2}sd_{NO2}}\sum([NO_2^-]_{model} - [NO_2^-]_{training})^2 +$$

$$\frac{w_{\delta NO3}}{n_{\delta NO3}sd_{\delta NO3}}\sum(\delta^{15}N_{NO3,model} - \delta^{15}N_{NO3,training})^2 + \frac{w_{\delta NO2}}{n_{\delta NO2}sd_{\delta NO2}}\sum(\delta^{15}N_{NO2,model} - \delta^{15}N_{NO2,training})^2$$

The w terms are weighting terms introduced to scale the contributions of the four observed parameters to equalize their contributions to the cost function. The n terms and standard deviation (sd) terms were used to normalize the contributions of each measurement type to the cost function. Each n term is equal to the number of each type of measurement in the training data set (e.g. the number of $[NO_3^-]$ data points = n_{NO3}). The sd term is equal to the standard deviation of all the measurements of a given type (e.g. the standard deviation of all the $[NO_3^-]$ data points within the training set).

In order to account for error in our model parameter estimates, we also iterated over several possible values for three of the most important isotope effects for processes in ODZs: NAR, NIR, and NXR (Table 3). We chose to iterate over these parameters rather than optimize them since there is a large range of estimates from the literature as to what these parameters might be. We assigned different possible values for each of these parameters (Table 3), resulting in 12 possible combinations.

5   The optimization protocol was performed for each of those combinations and unique optimized parameter sets were obtained. The parameter results were then averaged (final values, Table 2) and their spread is categorized as the error (error, Table 2).

3 Results

3.1 Global model-data comparison

The simulations of NO_2^- distribution and its isotopic composition are the most unique features of this model in comparison to

10   existing global models of the marine N cycle. As such, NO_2^- accumulation in ODZs is a feature that should be well-represented by the model in order to use it to test hypotheses about processes that control N cycling and loss in ODZs. Overall, we see NO_2^- accumulating at 200 m in the major ODZs of the Eastern Tropical North Pacific (ETNP), Eastern Tropical South Pacific (ETSP), and the Arabian Sea (AS) (Figure 2), which is consistent with observations and expected based on the low O_2 conditions found there. However, accumulation of NO_2^- in the model ETSP was lower than expected. The model also

15   accumulated NO_2^- in the Bay of Bengal, which is a low-O_2 region off the east coast of India that does not generally accumulate NO_2^- or support water column denitrification, but is thought to be near the "tipping point" for allowing N loss to occur (Bristow et al., 2016). Possible reasons for the underestimation of NO_2^- in the ETSP and overestimation in the Bay of Bengal will be discussed further in Section 4.2.

20   The model optimization described above yielded a set of isotope effects that best fit the global dataset of $[NO_3^-]$, $[NO_2^-]$, $\delta^{15}N_{NO3}$ and $\delta^{15}N_{NO2}$. The best fit was achieved for isotope effects of 13‰ for NO_3^- reduction (ε_{NAR}), 0‰ for NO_2^- reduction (ε_{NIR}), and -13‰ for NO_2^- oxidation (ε_{NXR}). Figure 3 shows the test set comparison for the global best-fit set of isotope effects overlaid with a 1:1 line, which the data would follow if there was perfect agreement between model results and observations. There is general agreement between model and observations, with most of the data clustering near the 1:1 lines. Agreement

25   between the observations and the training data are similar (Figure S4), indicating that we did not overfit the training data.

In the test set, there were some low $[O_2]$ points where our model $[NO_3^-]$ exceeded observations (Figure 3a, filled black circles); these are largely within the ETSP. In contrast, the Arabian Sea tended to show slightly lower modeled $[NO_3^-]$ than expected. The $[NO_2^-]$ accumulation (Figure 3b) and $\delta^{15}N_{NO3}$ signals (Figure 3c) in the ETSP were also generally too low compared with

30   observations. These signals are likely tied to insufficient NO_3^- reduction occurring in the model ETSP. Another consideration is that there may be a mismatch in resolution between the model and the space and time scales needed to resolve the high NO_2^- accumulations observed sporadically (Anderson et al., 1982; Codispoti et al., 1985; 1986).

Overall, the representation of $\delta^{15}N_{NO3}$ was fairly good (RMSE = 2.4‰), though there were a subset of points above $\delta^{15}N_{NO3} = 10‰$ where the modeled $\delta^{15}N_{NO3}$ exceeded the observed $\delta^{15}N_{NO3}$, and others where modeled $\delta^{15}N_{NO3}$ was lower than observations (Figure 3c). Many of the points with overestimated $\delta^{15}N_{NO3}$ were located within the Arabian Sea ODZ, where

5 there may be too much NO_3^- reduction occurring, leading to excess enrichment in ^{15}N-NO_3^-. As indicated above, the underestimated $\delta^{15}N_{NO3}$ points largely fell within the ETSP where we believe the model is underestimating NO_3^- reduction. The representation of $\delta^{15}N_{NO2}$ was also fairly good (RMSE = 8.6‰), though the modeled $\delta^{15}N_{NO2}$ was generally not low enough (Figure 3d), indicating an underestimated sink of 'heavy' NO_2^-.

3.2 Oxygen deficient zone model-data comparison using station profiles

10 To further investigate the distribution of model N species within the three main ODZs, we selected representative offshore grid boxes within each ODZ that contained observations to directly compare with model results in station profiles. Overall, the modeled NO_3^- and NO_2^- concentration and isotope profiles in the AS and ETNP were consistent with the observations, with $[NO_3^-]$ slightly underestimated in the Arabian Sea ODZ and overestimated in the ETSP (Figure 4). As $[O_2]$ goes to zero, the O_2-intolerant processes NAR, NIR, and AMX are released from inhibition. These processes result in a decrease in $[NO_3^-]$

15 (via NAR) which corresponds to an increase in $\delta^{15}N_{NO3}$, since NAR has a normal isotope effect. NO_2^- also starts to accumulate in the secondary NO_2^- maximum as a result of NAR. $\delta^{15}N_{NO2}$ is lower than $\delta^{15}N_{NO3}$ since light NO_2^- is preferentially created via NAR, and this discrepancy is further reinforced by the inverse isotope effect of NXR (Casciotti, 2009). These patterns are readily observed in the AS and ETNP, but were less apparent in the ETSP, where $[NO_3^-]$ depletion and $[NO_2^-]$ accumulation in the model were lower than observed. This could be due in part to the time-independent nature of this steady state inverse

20 model, which does not capture the effects of upwelling events in the ETSP on N supply and cycling (Canfield, 2006; Chavez and Messié, 2009).

In order to gauge the model results for N loss, we also calculated N*, a measure of the availability of DIN relative to PO_4^{3-} compared to Redfield ratio stoichiometry (N* = $[NO_3^-]$ + $[NO_2^-]$ − 16 * $[PO_4^{3-}]$; Deutsch et al., 2001). Negative N* values are

25 associated with N loss due to AMX or NIR or release of PO_4^{3-} from anoxic sediments (Noffke et al., 2012), while positive N* values are associated with input of new N through N_2 fixation (Gruber and Sarmiento, 1997). Although we did not model PO_4^{3-}, we used the modeled $[NO_3^-]$ and $[NO_2^-]$ together with World Ocean Atlas PO_4^{3-} data interpolated to the model grid to calculate N* resulting from the model. Both the AS and ETNP showed a decrease in model N* in the ODZ, as expected for water column N loss. Below the ODZ, N* increased again and returned to expected deep water values. Modeled N* in the ETSP,

30 however, did not follow the observed trend, consistent with an underestimate of N loss in the model ETSP.

Though the global best fit isotope effects for NAR, NIR, and NXR produced good agreement to the data in general, the isotope effects that best fit individual ODZ regions differed when the cost function was restricted to observations from a given ODZ.

For the ETSP, the best fit isotope effects were the same as the previously stated global best fit. For the AS, the best fit isotope effects were ε_{NAR} = 13‰, ε_{NIR} = 0‰, and ε_{NXR} = -32‰. For the ETNP, the best fit isotope effects were ε_{NAR} = 13‰, ε_{NIR} = 15‰, and ε_{NXR} = -32‰, though the performance is only marginally better than with ε_{NIR} = 0‰. The lower (more inverse) value for ε_{NXR} resulted in higher $\delta^{15}N_{NO3}$ and lower $\delta^{15}N_{NO2}$, which better fit the ODZ $\delta^{15}N_{NO2}$ data compared to the global best fit

5 ε_{NXR} = -13‰. These results are consistent with earlier isotope modeling studies in the ETSP (Casciotti et al., 2013; Peters et al., 2016; Peters et al., 2018b) and in the Arabian Sea (Martin and Casciotti, 2017). Although, in the Arabian Sea, modeled $\delta^{15}N_{NO3}$ were too high in the ODZ, likely in part due to overpredicted rates of NAR, which also resulted in lower modeled [NO_3^-] (Figure 4).

3.3 Model-data comparison in GEOTRACES sections

10 We also investigated the agreement between global best fit model concentration and isotope distributions with data from two GEOTRACES cruise sections: GP16 in the South Pacific, and GA03 in the North Atlantic. For GP16, we see that [NO_3^-] is low in surface waters and increases to a mid-depth maximum between 1000-2000 m. The highest [NO_3^-] are found at mid-depth in the eastern boundary of the section. The model reproduces the general patterns, matching observations fairly well in the surface waters, but diverges below 500 m (Figure 5). Although the patterns are generally correct, insufficient NO_3^- is

15 accumulated in the deep waters of the model Pacific. This could be due to an underestimate of preformed NO_3^- (over estimate of assimilation in the Southern Ocean), or inadequate supply of organic matter to be remineralized at depth. In the Southern Ocean, model surface [NO_3^-] are 5-10 μM lower than observations (Figure S5), which could be enough to explain the lower than expected [NO_3^-] in the deep Pacific, which is largely sourced from the Southern Ocean (Rafter et al., 2013; Sigman et al., 2009; Peters et al., 2018a,b).

In the GP16 section, we also see that there are elevated $\delta^{15}N_{NO3}$ values in the model surface waters and in the ETSP ODZ (Figure 5d), as expected from observations (Figure 5c). However, we can also see that the insufficient depletion of NO_3^- and increase in $\delta^{15}N_{NO3}$ in the ETSP ODZ (Figure 5b and d) extends beyond the single grid box highlighted earlier (Figure 4). The less than expected increase of $\delta^{15}N_{NO3}$ in the ETSP ODZ and the upper thermocline in the eastern part of the section is consistent

25 with an underestimate of NO_3^- reduction. In GP16 we were also able to compare modelled and observed [NO_2^-] and $\delta^{15}N_{NO2}$ (Figure S6). Patterns of modeled [NO_2^-] and $\delta^{15}N_{NO2}$ showed accumulation of NO_2^- in the ODZ, with an appropriate $\delta^{15}N_{NO2}$ value (Figure S6). Although, generally lower modeled concentrations of NO_2^- in the ODZ also support an underestimate of NAR (Figure S6).

30 Surface $\delta^{15}N_{NO3}$ values were also not as high in the model as in the observations (Figure 5), which could result from insufficient NO_3^- assimilation or too low supplied $\delta^{15}N_{NO3}$ (Peters et al., 2018a). However, we do see a similar depth range for high surface $\delta^{15}N_{NO3}$ and a local $\delta^{15}N_{NO3}$ minimum between the surface and ODZ propagating westward in both the model and observations,

indicating that the physical and biogeochemical processes affecting $\delta^{15}N_{NO3}$ are represented by the model. Additionally, the model shows slightly elevated $\delta^{15}N_{NO3}$ in the thermocline depths (200-500m) west of the ODZ, which is consistent with the observations (Figure 5c), though not of the correct magnitude. This is partly related to the muted ODZ signal as mentioned above and its lessened impact on thermocline $\delta^{15}N_{NO3}$ across the basin. Peters et al. (2018a) and Rafter et al. (2013) also

5   postulated that these elevated $\delta^{15}N_{NO3}$ values were in part driven by remineralization of organic matter with high $\delta^{15}N$. The $\delta^{15}N$ of sinking PON in the model (6-10‰) was similar to those observed in the south Pacific (Raimbault et al., 2008), as well as those predicted from other N isotope studies (Rafter et al., 2013; Peters et al., 2018). The model also shows slightly elevated $\delta^{15}N_{NO3}$ in the intermediate depths (500-1500m), which is consistent with observations, again reflecting remineralization of PON with $\delta^{15}N$ greater than mean ocean $\delta^{15}N_{NO3}$. Overall, the patterns of $\delta^{15}N_{NO3}$ are correct but the magnitudes of isotopic

10   variation are muted, largely due to the lack of N loss in the ODZ and modeled surface $\delta^{15}N_{NO3}$ values that are lower than observations. The simplification of NH_4^+ dynamics in the model could also contribute to underestimation of $\delta^{15}N_{NO3}$ values if there was a large flux of ^{15}N-enriched NH_4^+ from sediments (Granger et al., 2011), or if ^{15}N-depleted NH_4^+ was preferentially transferred to the N_2 pool via anammox. While the isotope effect on NH_4^+ during anammox (Brunner et al., 2013) is indeed higher than that applied here, we chose to balance this with a low isotope effect during aerobic NH_4^+ oxidation (Table 1).

In the north Atlantic along GEOTRACES section GA03, we see good agreement between the observed and modeled $[NO_3^-]$ (Figure 6). There is generally low surface $[NO_3^-]$ with a distinct area of high $[NO_3^-]$ propagating from near the African coast. Deep water (> 2000 m) $[NO_3^-]$ is lower than we see in the Pacific section, and the model matches well with the Atlantic observations. Again, there is not quite enough NO_3^- present in Southern Ocean-sourced intermediate waters (500-1500 m;

20   Marconi et al., 2015). Modeled $\delta^{15}N_{NO3}$ values at first glance appear higher than observed values at the surface (Figure 6). However, many of the surface $[NO_3^-]$ were below the operating limit for $\delta^{15}N_{NO3}$ analysis and were not determined. Focusing on areas where both measurements and model results are present yields excellent agreement. For example, we do see low $\delta^{15}N_{NO3}$ values in upper thermocline waters in both the model and observations, likely corresponding to low $\delta^{15}N$ contributions from N_2 fixation that is remineralized at depth and accumulated in North Atlantic Central Water (Marconi et al., 2015; Knapp

25   et al., 2008). The model input includes significant rates of N_2 fixation in the North Atlantic that are consistent with this observation (Martin et al., in review). However, rates of N deposition in the North Atlantic are also fairly high and can contribute to the low $\delta^{15}N$ signal (Knapp et al., 2008). In our model, atmospheric N deposition contributed between 0-50% of N input along the cruise track.

4 Discussion

4.1 Assumption checks

As previously mentioned (Section 2.3), organic N and DIN were modeled separately in order to introduce dependence on both organic N and substrate availability for the heterotrophic processes NAR and NIR. These separate model runs require several assumptions to be made regarding the processes that impact both organic N and DIN, namely assimilation and remineralization.

The first assumption is that the rates of N assimilation are equal between the organic N and DIN model runs. The organic N model run uses World Ocean Atlas surface $[NO_3^-]$ to estimate the contribution of DIN assimilation to the production of organic N, whereas the DIN model run uses modeled $[NO_3^-]$ and $[NO_2^-]$ to estimate DIN removal via assimilation. Though these two methods utilized the same rate constants for assimilation, differences in [DIN] could cause some discrepancies between the overall rates. Analysis of the results revealed that slightly more overall DIN assimilation occurred in the DIN model run than organic N produced in the organic N model (Figure S7). This could be due in part to assimilation of NO_2^- in the top two boxes of the DIN model, since NO_2^- assimilation is unaccounted for in the organic N model. This is largely an issue in the oligotrophic gyres, where surface $[NO_3^-]$ is very low and NO_2^- accumulates to low but non-zero concentrations (Figure 2). Assimilation of NO_2^- accounts for a significant fraction of DIN assimilation in these regions, but the overall assimilation rates there are low and the resulting influence on the whole system is also low. In other regions, modeled surface $[NO_3^-]$ may be higher than the World Ocean Atlas surface $[NO_3^-]$ that are supplied to the organic N model, which would result in higher assimilation rates in the DIN model run. Indeed, points at which the DIN assimilation rates are higher than the organic N production rates do tend to have modeled $[NO_3^-]$ that was higher than observed $[NO_3^-]$ (Figure S7). Likewise, points with relatively lower DIN assimilation had modeled $[NO_3^-]$ less than observed $[NO_3^-]$. However, the majority of DIN assimilation estimates were within 10 µM/yr of the organic N production estimates, with an average offset of approximately 3.5% compared to DIN assimilation. The total global assimilation rates were within 0.4%, with some spatially variable differences due to offset between surface $[NO_3^-]$ and modeled $[NO_3^-]$. However we find that the World Ocean Atlas surface NO_3^- values are fairly well represented by our modeled surface NO_3^- (Figure S5). We conclude that though the assimilation rates are not identical in the organic N and DIN model runs, the discrepancy in modeled DIN assimilation is less than 0.1%, and there is unlikely to be significant creation or loss of N as a result of the split model.

4.2 Model dependency on input O_2

The modeled concentration and isotope profiles for the ETSP, unlike in the AS and ETNP, reflected an underestimation of water column denitrification in the best-fit model. In ETSP $[NO_3^-]$ measurements, there is a clear deficit in $[NO_3^-]$, coincident with the secondary NO_2^- maximum and N* minimum (Figure 4). In our modeled profiles, this NO_3^- deficit is missing, and although a secondary NO_2^- maximum is present, its magnitude is lower than observed (Figure 4). The model also does not capture the negative N* excursion (Figure 4), which we think reflects a model underestimation of NAR and NIR in the ETSP.

The cause of this missing denitrification is likely to be poor representation of the ETSP O_2 conditions in the model grid space. Since our model grid is fairly coarse (2˚x2˚), only a few boxes within the ETSP had averaged [O_2] below the thresholds that would allow processes such as NAR and NIR to occur. The anoxic region of the ETSP is adjacent to the coast and not as spatially extensive as in the AS and ETNP (Figure S8); therefore, this region in particular was less compatible with the model grid. In order to test whether the parameterization of O_2 dependence was the cause of the low N loss, we ran the model using the globally optimized parameters (Table 3) but with higher O_2 thresholds (15 μM) for NAR, NIR, and AMX (Table 1). This extended the region over which ODZ processes could occur and resulted in an increase in water column N loss from 6 to 32 Tg N/yr in the ETSP, which is more consistent with previous estimates (DeVries et al., 2012; Deutsch et al., 2001). This change also stimulated the development of a NO_3^- deficit, larger secondary NO_2^- maximum, and N* minimum within the ODZ (Figure 7).

As previously mentioned (Section 3.1), modeled [NO_2^-] in the Bay of Bengal is higher than observations. The accumulation of NO_2^- here in the model is likely due to O_2 concentrations falling below the set threshold for NAR but above the threshold for NIR, so NO_2^- can accumulate via NAR but cannot be consumed via NIR. Although AMX and NXR occur there, the modeled rates of their NO_2^- consumption are rather low, which in combination with high rates of NAR leads to more NO_2^- being produced than consumed. This is in contrast to observations that NO_2^- production is tightly matched with NO_2^- oxidation in the Bay of Bengal, which limits NO_2^- accumulation and N loss there (Bristow et al., 2016). The fact that the model over predicts NAR in the Arabian Sea may also be connected with over-prediction of NAR in the Bay of Bengal. It is possible that the oxygen thresholds for ODZ processes are not the same in all ODZs, and further work on oxygen sensitivities of N cycle processes will be addressed in a companion study (Martin et al., in review).

5 Conclusions

A global inverse ocean model was modified to include ^{14}N and ^{15}N in both NO_3^- and NO_2^- as state variables. Adding the processes required to describe the cycling of NO_2^- in the global ocean, including oxic and anoxic processes, resulted in a globally representative distribution of [NO_3^-], [NO_2^-], $\delta^{15}N_{NO3}$, and $\delta^{15}N_{NO2}$. In particular, the patterns of variation in both oxic and anoxic waters are generally consistent with observations, though some magnitudes of variation were somewhat muted by the model. This could be due to an underestimation of a process rate, due to parameterization or model resolution, or an underestimation of the isotope effect involved.

Importantly, we were able to generate a roughly balanced steady-state ocean N budget without the need for an artificial restoring force. The [NO_3^-] and [NO_2^-] distributions that were required to achieve this roughly balanced budget are well within the range of observed values. Some interesting take-home messages from this work are: 1) a relatively low isotope effect for NO_3^- reduction ($\varepsilon_{NAR} = 13‰$) gives a good fit to $\delta^{15}N_{NO3}$ data, similar to that concluded in some recent studies (Marconi et al.,

2017; Bourbonnais et al., 2015; Casciotti et al., 2013), 2) low O_2 half-saturation constants for NO_2^- oxidation allowing NO_2^- oxidation to occur in parallel with NO_3^- reduction, NO_2^- reduction, and anammox were needed to achieve the correct distributions of NO_3^-, NO_2^-, and their isotopes, in the oceans water column ODZs.

5   Though we have been able to adequately represent and assess N cycling in ODZs, there are many areas in which this model could be improved in order to expand its usefulness. Improving resolution of the model, particularly in coastal regions where there are steep gradients in nutrient and O_2 concentrations, would improve the accuracy of the model in regions such as the ETSP. Further, in regions that have high seasonal or interannual variability, an annually averaged steady-state model may not represent some important temporal dynamics. While we attempted to account for seasonal variation in the strength of the ODZs

10   through use of monthly O_2 climatologies, we did not simulate seasonal variations in net primary production and the strength of the biological pump. Variations in these parameters are likely to drive variations in N loss (Kalvelage et al., 2013; Ward, 2013; Babbin et al., 2014).

In addition to the dependency on external static nutrient and parameter fields, this N cycle model is highly dependent on isotope

15   effects for N cycle processes. Previous work has shown that the laboratory-derived isotope effects for some N cycle processes are not the same as their expressed isotope effects in environmental samples or under conditions relevant to environmental samples (Casciotti et al., 2013; Bourbonnais et al., 2015; Buchwald et al., 2015; Kritee et al., 2012; Marconi et al., 2017a). Further probing the isotope effects using an inverse model such as this could provide insight into the expressed isotope effects that should be used in other modeling efforts involving field data. As presented in Section 3.1, the larger magnitude isotope

20   effect for NO_2^- oxidation best fit the ETNP and Arabian Sea ODZs, where most of the ODZ volume resided. However, most model $\delta^{15}N_{NO2}$ values still do not reach the lowest values observed on the edges of marine ODZs, indicating that further work is needed to understand the expression of these isotope effects.

The larger isotope effects resulted in better fits to observations of $\delta^{15}N$ and DIN concentrations with lower rates of N cycling.

25   This reinforces the importance of obtaining realistic isotope effect estimates for each process that are relevant on an environmental scale. Additionally, this highlights the need for critical consideration of isotope effects used in N cycle models that use isotope balance to predict N cycling rates. Though isotopes provide us a useful tool to assess the relative contributions of different processes, these estimates are highly subject to the isotope effects employed. Also, as illustrated by the regional optimizations, the isotope effect for a given process may vary, or be expressed differently, in different regions.

This model provides an excellent framework for further testing hypotheses about controls on the marine N inventory and cycling of N on a global scale. The distribution and sensitivities of N cycle rates resulting from this model will be explored in a companion manuscript (Martin et al., in review). Incorporation of variable environmental input data, such as temperature, productivity, and [O_2], could also help us predict how the N cycle might be affected by past and future environmental changes.

Code availability

Model code and model output from the three optimal ODZ isotope effect combinations, including the global best fit, are available in the Stanford Digital Repository (https://purl.stanford.edu/hr045dx8661).

Author contribution

5   KLC, FP, and TSM designed the study. TSM and FP constructed the model. TSM and KLC analysed and interpreted the results. TSM, KLC, and FP wrote the manuscript.

Competing interests

The authors declare that they have no conflict of interest.

Acknowledgements

10   Thanks to Patrick Rafter for sharing a pre-publication version of his NO_3^- isotope database. Thanks to Tim Davis for guidance on sparse matrix solvers. Thanks to Tim DeVries for helpful discussions about earlier versions of the inverse model. Thanks to Kevin Arrigo and Leif Thomas for comments on an earlier draft of this manuscript. This work was partly supported by NSF Chemical Oceanography grant 1657868 to KLC.

References

15   1.   Anderson, J. J., Okubo, A., Robbins, A. S. and Richards, F. A.: A model for nitrate distributions in oceanic oxygen minimum zones, Deep-Sea Res., 29, 1113-1140, doi:10.1016/0198-0149(82)90031-0, 1982.

2.   Babbin, A. R., Keil, R. G., Devol, A. H. and Ward, B. B.: Organic Matter Stoichiometry, Flux, and Oxygen Control Nitrogen Loss in the Ocean, Science, 344, 406–408, doi:10.1126/science.1248364, 2014.

3.   Babbin, A. R,, Peters, B. D., Mordy, C. W., Widner, B., Casciotti, K. L. and Ward, B. B.: Multiple metabolisms

20   constrain the anaerobic nitrite budget in the Eastern Tropical South Pacific, Global Biogeochem. Cy., 31, 258-271, doi:10.1002/2016GB005407, 2017.

4.   Berelson, W. M.: Particle settling rates increase with depth in the ocean, Deep-Sea Res. Pt. II, 49, 237-251. doi:10.1016/S0967-0645(01)00102-3, 2002.

5.   Bianchi, D., Dunne, J. P., Sarmiento, J. L. and Galbraith, E. D.: Data-based estimates of suboxia, denitrification, and

25   N_2O production in the ocean and their sensitivities to dissolved O_2, Global Biogeochem. Cy., 26, 1-13, doi:10.1029/2011GB004209, 2012.

6. Bohlen, L., Dale, A. W. and Wallmann, K.: Simple transfer functions for calculating benthic fixed nitrogen losses and C:N:P regeneration ratios in global biogeochemical models, Global Biogeochem. Cy, 26, GB3029, doi:10.1029/2011GB004198, 2012.

7. Bonin, P., Gilewicz, M. and Bertrand, J. C.: Effects of oxygen on each step of denitrification on Pseudomonas nautica, Can. J. Microbiol., 35, 1061-1064, doi:10.1139/m89-177, 1989.

8. Bourbonnais, A., Altabet, M. A., Charoenpong, C. N., Larkum, J., Hu, H., Bange, H. W. and Stramma, L.: N-loss isotope effects in the Peru oxygen minimum zone studied using a mesoscale eddy as a natural tracer experiment, Global Biogeochem. Cy., 29, 793-811, doi:10.1002/2013GB004679, 2015.

9. Brandes, J. A. and Devol, A. H.: Isotopic fractionation of oxygen and nitrogen in coastal marine sediments, Geochim. Cosmochim. Ac., 61, 1793-1801, doi:10.1016/S0016-7037(97)00041-0, 1997.

10. Brandes, J. A. and Devol, A. H.: A global marine-fixed nitrogen isotopic budget: Implications for Holocene nitrogen cycling, Global Biogeochem. Cy., 16, 67-1-67-14, doi:10.1029/2001GB001856, 2002.

11. Bristow, L. A., Dalsgaard, T., Tiano, L., Mills, D. B., Bertagnolli, A. D., Wright, J. J., Hallam, S. J., Ulloa, O., Canfield, D. E., Revsbech, N. P. and Thamdrup, B.: Ammonium and nitrite oxidation at nanomolar oxygen concentrations in oxygen minimum zone waters, P. Natl. Acad. Sci. USA, 113, 10601-10606, doi:10.1073/pnas.1600359113, 2016.

12. Bristow, L. A., Callbeck, C. M., Larsen, M., Altabet, M. A., Dekaezemacker, J., Forth, M., Gauns, M., Glud, R. N., Kuypers, M. M. M., Lavik, G., Milucka, J., Naqvi, S. W. A., Pratihary, A., Revsbech, N. P., Thamdrup, B., Treusch, A. H. and Canfield, D. E.: N_2 production rates limited by nitrite availability in the Bay of Bengal oxygen minimum zone, Nat. Geosci., 10, 24-29, doi:10.1038/ngeo2847, 2017.

13. Brown, Z. W., Casciotti, K. L., Pickart, R. S., Swift, J. H. and Arrigo, K. R.: Aspects of the marine nitrogen cycle of the Chukchi Sea shelf and Canada Basin, Deep. Res. Part II Top. Stud. Oceanogr., 118, 73–87, doi:10.1016/j.dsr2.2015.02.009, 2015.

14. Brunner, B., Contreras, S., Lehmann, M. F., Matantseva, O., Rollog, M., Kalvelage, T., Klockgether, G., Lavik, G., Jetten, M. S. M., Kartal, B. and Kuypers, M. M. M.: Nitrogen isotope effects induced by anammox bacteria, P. Natl. Acad. Sci. USA, 110, 18994-18999, doi:10.1073/pnas.1310488110, 2013.

15. Bryan, B. A., Shearer, G., Skeeters, J. L. and Kohl, D. H.: Variable expression of the nitrogen isotope effect associated with denitrification of nitrite, J. Biol. Chem., 258, 8613-8617, 1983.

16. Buchwald, C. and Casciotti, K. L.: Oxygen isotopic fractionation and exchange during bacterial nitrite oxidation, Limnol. Oceanogr., 55, 1064-1074, doi:10.4319/lo.2010.55.3.1064, 2010.

17. Buchwald, C., Santoro, A. E., Stanley, R. H. R. and Casciotti, K. L.: Nitrogen cycling in the secondary nitrite maximum of the eastern tropical North Pacific off Costa Rica, Global Biogeochem. Cy., 29, 2061-2081, doi:10.1002/2015GB005187, 2015.

18. Buesseler, K. O. and Boyd, P. W.: Shedding light on processes that control particle export and flux attenuation in the twilight zone of the open ocean, Limnol. Oceanogr., 54, 1210-1232, doi:10.4319/lo.2009.54.4.1210, 2009.

19. Buesseler, K. O., Trull, T. W., Steinberg, D. K., Silver, M. W., Siegel, D. A., Saitoh, S. -I., Lamborg, C. H., Lam, P. J., Karl, D. M., Jiao, N. Z., Honda, M. C., Elskens, M., Dehairs, F., Brown, S. L., Boyd, P. W., Bishop, J. K. B. and Bidigare, R. R.: VERTIGO (VERtical Transport In the Global Ocean): A study of particle sources and flux attenuation in the North Pacific, Deep-Sea Res. Pt. II, 55, 1522-1539, doi:10.1016/j.dsr2.2008.04.024, 2008.

20. Canfield, D. E.: Models of oxic respiration, denitrification and sulfate reduction in zones of coastal upwelling, Geochim. Cosmochim. Acta, 70, 5753–5765, doi:10.1016/j.gca.2006.07.023, 2006.

21. Capone, D. G., Burns, J. A., Montoya, J. P., Subramaniam, A., Mahaffey, C., Gunderson, T., Michaels, A. F. and Carpenter, E. J.: Nitrogen fixation by Trichodesmium spp.: An important source of new nitrogen to the tropical and subtropical North Atlantic Ocean, Global Biogeochem. Cy., 19, GB2024, doi:10.1029/2004GB002331, 2005.

22. Carpenter, E. J., Harvey, H. R., Brian, F. and Capone, D. G.: Biogeochemical tracers of the marine cyanobacterium Trichodesmium, Deep-Sea Res. Pt. I, 44, 27-38, doi:10.1016/S0967-0637(96)00091-X, 1997.

23. Casciotti, K. L.: Inverse kinetic isotope fractionation during bacterial nitrite oxidation, Geochim. Cosmochim. Ac., 73, 2061-2076, doi:10.1016/j.gca.2008.12.022, 2009.

24. Casciotti, K. L., Trull, T. W., Glover, D. M. and Davies, D.: Constraints on nitrogen cycling at the subtropical North Pacific Station ALOHA from isotopic measurements of nitrate and particulate nitrogen, Deep-Sea Res. Pt. II, 55, 1661-1672, doi:10.1016/j.dsr2.2008.04.017, 2008.

25. Casciotti, K. L., Buchwald, C. and McIlvin, M.: Implications of nitrate and nitrite isotopic measurements for the mechanisms of nitrogen cycling in the Peru oxygen deficient zone, Deep-Sea Res. Pt. I, 80, 78-93, doi:10.1016/j.dsr.2013.05.017, 2013.

26. Chavez, F. P. and Messié, M.: A comparison of Eastern Boundary Upwelling Ecosystems, Prog. Oceanogr., 83, 80–96, doi:10.1016/j.pocean.2009.07.032, 2009.

27. Chien, C-T., Mackey, K. R. M., Dutkiewicz, S., Mahowald, N. M., Prospero, J. M. and Paytan, A.: Effects of African dust deposition on phytoplankton in the western tropical Atlantic Ocean off Barbados, Global Biogeochem. Cy., 30, 716-734, doi:10.1002/2015GB005334, 2016.

28. Codispoti, L. A.: Phosphorus vs. Nitrogen limitation of new and export production, in: Productivity of the Oceans: Present and Past. Vol 44., John Wiley & Sons Ltd., 377-394, 1989.

29. Codispoti, L. A. and Christensen, J. P.: Nitrification, denitrification and nitrous oxide cycling in the eastern tropical South Pacific ocean, Mar. Chem., 16, 277-300, doi:10.1016/0304-4203(85)90051-9, 1985.

30. Codispoti, L. A., Friederich, G. E., Packard T. T., Glover, H. E., Kelly, P. J., Spinrad, R. W., Barber, R. T., Elkins, J. W., Ward, B. B., Lipschultz, F. and Lostaunau, N.: High Nitrite Levels off Northern Peru: A Signal of Instability in the Marine Denitrification Rate, Science, 233, 1200-1202, doi:10.1126/science.233.4769.1200, 1986.

31. Codispoti, L. A., Brandes, J. A., Christensen, J. P., Devol, A. H., Naqvi, S. W. A, Paerl, H. W. and Yoshinari, T.: The oceanic fixed nitrogen and nitrous oxide budgets: Moving targets as we enter the anthropocene?, Sci. Mar., 65, 80-105, doi:10.3989/scimar.2001.65s285, 2001.

32. Dalsgaard, T., Stewart, F. J., Thamdrup, B., De Brabandere, L., Revsbech, N. P., Ulloa, O., Canfield, D. E. and DeLong, E. F.: Oxygen at nanomolar levels reversibly suppresses process rates and gene expression in anammox and denitrification in the oxygen minimum zone off Northern Chile, MBio, 5, e01966-14, doi:10.1128/mBio.01966-14, 2014.

33. Dentener, F., Drevet, J., Lamarque, J. F., Bey, I., Eickhout, B., Fiore, A. M., Hauglustaine, D., Horowitz, L. W., Krol, M., Kulshrestha, U. C., Lawrence, M., Galy-Lacaux, C., Rast, S., Shindell, D., Stevenson, D., Van Noije, T., Atherton, C., Bell, N., Bergman, D., Butler, T., Cofala, J., Collins, B., Doherty, R., Ellingsen, K., Galloway, J., Gauss, M., Montanaro, V., Müller, J. F., Pitari, G., Rodriguez, J., Sanderson, M., Solmon, F., Strahan, S., Schultz, M., Sudo, K., Szopa, S. and Wild, O.: Nitrogen and sulfur deposition on regional and global scales: A multimodel evaluation, Global Biogeochem. Cy., 20, GB4003, doi:10.1029/2005GB002672, 2006.

34. Deutsch, C., Gruber, N., Key, R. M., Sarmiento, J. L. and Ganachaud, A.: Denitrification and N_2 fixation in the Pacific Ocean, Global Biogeochem. Cy., 15, 483-506, doi:10.1029/2000GB001291, 2001.

35. Deutsch, C., Sarmiento, J. L., Sigman, D. M., Gruber, N. and Dunne, J. P.: Spatial coupling of nitrogen inputs and losses in the ocean, Nature, 445, 163-167, doi:10.1038/nature05392, 2007.

36. DeVries, T. and Primeau, F.: Dynamically and Observationally Constrained Estimates of Water-Mass Distributions and Ages in the Global Ocean, J. Phys. Oceanogr., 41, 2381-2401, doi:10.1175/JPO-D-10-05011.1, 2011.

37. DeVries, T., Deutsch, C., Rafter, P. A. and Primeau, F.: Marine denitrification rates determined from a global 3-D inverse model, Biogeosciences, 10, 2481-2496, doi:10.5194/bg-10-2481-2013, 2013.

38. Dunne, J. P., Armstrong, R. A., Gnanadesikan, A. and Sarmiento, J. L.: Empirical and mechanistic models for the particle export ratio, Global Biogeochem. Cy., 19, GB4026, doi:10.1029/2004GB002390, 2005.

39. Follows, M. J., Dutkiewicz, S., Grant, S. and Chisholm, S. W.: Emergent Biogeography of Microbial Communities in a Model Ocean, Science, 315, 1843-1846, doi:10.1126/science.1138544, 2007.

40. Frey, C., Hietanen, S., Jürgens, K., Labrenz, M. and Voss, M.: N and O isotope fractionation in nitrate during chemolithoautotrophic denitrification by Sulfurimonas gotlandica, Environ. Sci. Technol., 48(22), 13229–13237, doi:10.1021/es503456g, 2014.

41. Fuchsman, C. A., Devol, A. H., Casciotti, K. L., Buchwald, C., Chang, B. X. and Horak, R. E. A.: An N isotopic mass balance of the Eastern Tropical North Pacific Oxygen Deficient Zone, Deep-Sea Res. Pt. II, doi:10.1016/j.dsr2.2017.12.013, 2017.

42. Galloway, J. N., Dentener, F. J., Capone, D. G., Boyer, E. W., Howarth, R. W., Seitzinger, S. P., Asner, G. P., Cleveland, C. C., Green, P. A., Holland, E. A., Karl, D. M., Michaels, A. F., Porter, J. H., Townsend, A. R. and

Vörösmarty, C. J.: Nitrogen cycles: past, present, and future, Biogeochemistry, 70, 153-226, doi:10.1007/s10533-004-0370-0, 2004.

43. Garcia, H. E., Boyer, T. P., Locarnini, R. A., Boyer, T. P., Antonov, J. I., Mishonov, A. V., Baranova, O. K., Zweng, M. M., Reagan, J. R. and Johnson, D. R.: World Ocean Atlas 2013. Volume 3: dissolved oxygen, apparent oxygen utilization, and oxygen saturation, NOAA Atlas NESDIS 75, 27 pp., 2013.

44. Garcia, H. E., Locarnini, R. A., Boyer, T. P., Antonov, J. I., Baranova, O. K., Zweng, M. M., Reagan, J. R. and Johnson, D. R.: World Ocean Atlas 2013. Volume 4: Dissolved inorganic nutrients (phosphate, nitrate, silicate), NOAA Atlas NESDIS 76, 25 pp., 2013.

45. Gaye, B., Nagel, B., Dähnke, K., Rixen, T. and Emeis, K-C.: Evidence of parallel denitrification and nitrite oxidation in the ODZ of the Arabian Sea from paired stable isotopes of nitrate and nitrite. Global Biogeochem. Cy. 27, 1059-1071, doi:10.1002/2011GB004115, 2013.

46. Granger, J., Sigman, D. M., Lehmann, M. F. and Tortell, P. D.: Nitrogen and oxygen isotope fractionation during dissimilatory nitrate reduction by denitrifying bacteria, Limnol. Oceanogr., 53, 2533-2545, doi:10.4319/lo.2008.53.6.2533, 2008.

47. Granger, J., Sigman, D. M., Rohde, M. M., Maldonado, M. T. and Tortell, P. D.: N and O isotope effects during nitrate assimilation by unicellular prokaryotic and eukaryotic plankton cultures, Geochim. Cosmochim. Ac., 74, 1030-1040, doi:10.1016/j.gca.2009.10.044, 2010.

48. Granger, J., Prokopenko, M. G., Sigman, D. M., Mordy, C. W., Morse, Z. M., Morales, L. V., Sambrotto, R. N. and Plessen, B.: Coupled nitrification-denitrification in sediment of the eastern Bering Sea shelf leads to15N enrichment of fixed N in shelf waters, J. Geophys. Res. Ocean., 116(11), 1–18, doi:10.1029/2010JC006751, 2011.

49. Gruber, N. The Dynamics of the Marine Nitrogen Cycle and its Influence on Atmospheric CO_2 Variations, in: The Ocean Carbon Cycle and Climate, Springer, Netherlands, 2004.

50. Gruber, N. The Marine Nitrogen Cycle: Overview and Challenges, in: Nitrogen in the Marine Environment. Capone, D. G., Bronk, D. A., Mulholland, M. R., Carpenter, E. J., eds. Elsevier, 2008.

51. Gruber, N. and Galloway, J. N.: An Earth-system perspective of the global nitrogen cycle., Nature, 451(7176), 293–6, doi:10.1038/nature06592, 2008.

52. Gruber, N. and Sarmiento, J. L.: Global patterns of marine nitrogen fixation and denitrification, Global Biogeochem. Cy., 11, 235-266, doi:10.1029/97GB00077, 1997.

53. Harding, K., Turk-Kubo, K. A., Sipler, R. E., Mills, M. M., Bronk, D. A. and Zehr, J. P.: Symbiotic unicellular cyanobacteria fix nitrogen in the Arctic Ocean, Proc. Natl. Acad. Sci., 201813658, doi:10.1073/pnas.1813658115, 2018.

54. Hastings, M. G., Jarvis, J. C. and Steig, E. J.: Anthropogenic Impacts on Nitrogen Isotopes of Ice-Core Nitrate, Science, 324, 1288, doi:10.1126/science.1170510, 2009.

55. Hoering, T. C. and Ford, H. T.: The Isotope Effect in the Fixation of Nitrogen by Azotobacter, J. Am. Chem. Soc., 82, 376-378. doi:10.1021/ja01487a031, 1960.

56. Holl, C. M. and Montoya, J. P.: Interactions between nitrate uptake and nitrogen fixation in continuous cultures of the marine diazotroph Trichodesmium (Cyanobacteria), J. Phycol., 41, 1178-1183, doi:10.1111/j.1529-8817.2005.00146.x, 2005.

57. Hu, H., Bourbonnais, A., Larkum, J., Bange, H. W. and Altabet, M. A.: Nitrogen cycling in shallow low-oxygen coastal waters off Peru from nitrite and nitrate nitrogen and oxygen isotopes, Biogeosciences, 13, 1453-1468, doi:10.5194/bg-13-1453-2016, 2016.

58. Jensen, M. M., Kuypers, M. M. M., Lavik, G. and Thamdrup, B.. Rates and regulation of anaerobic ammonium oxidation and denitrification in the Black Sea, Limnol. Oceanogr., 53, 23-36, doi:10.4319/lo.2008.53.1.0023, 2008.

59. Kalvelage, T., Jensen, M. M., Contreras, S., Revsbech, N. P., Lam, P., Günter, M., LaRoche, J., Lavik, G. and Kuypers, M. M. M.: Oxygen Sensitivity of Anammox and Coupled N-Cycle Processes in Oxygen Minimum Zones, PLoS One, 6, e29299, doi:10.1371/journal.pone.0029299, 2011.

60. Kalvelage, T., Lavik, G., Lam, P., Contreras, S., Arteaga, L., Loscher, C. R., Oschlies, A., Paulmier, A., Stramma, L. and Kuypers, M. M. M.: Nitrogen cycling driven by organic matter export in the South Pacific oxygen minimum zone, Nat. Geosci., 6(3), 228–234, doi:10.1038/ngeo1739, 2013.

61. Knapp, A. N., DiFiore, P. J., Deutsch, C., Sigman, D. M. and Lipschultz, F.: Nitrate isotopic composition between Bermuda and Puerto Rico: Implications for N_2 fixation in the Atlantic Ocean, Global Biogeochem. Cy., 22, GB3014, doi:10.1029/2007GB003107, 2008.

62. Knapp, A. N., Sigman, D. M., Lipschultz, F., Kustka, A. B. and Capone, D. G.: Interbasin isotopic correspondence between upper-ocean bulk DON and subsurface nitrate and its implications for marine nitrogen cycling, Global Biogeochem. Cy., 25, GB4004, doi:10.1029/2010GB003878, 2011.

63. Kritee, K., Sigman, D. M., Granger, J., Ward, B. B., Jayakumar, A. and Deutsch, C.: Reduced isotope fractionation by denitrification under conditions relevant to the ocean, Geochim. Cosmochim. Ac., 92, 243-259, doi:10.1016/j.gca.2012.05.020, 2012.

64. Kuypers, M. M. M., Lavik, G., Woebken, D., Schmid, M., Fuchs, B. M., Amann, R., Jorgensen, B. B. and Jetten, M. S. M.: Massive nitrogen loss from the Benguela upwelling system through anaerobic ammonium oxidation, P. Natl. Acad. Sci. USA, 102, 6478-6483, doi:10.1073/pnas.0502088102, 2005.

65. Landolfi, A., Kähler, P., Koeve, W. and Oschlies, A.: Global marine N2 fixation estimates: From observations to models, Front. Microbiol., 9(SEP), 1–8, doi:10.3389/fmicb.2018.02112, 2018.

66. Lavik, G., Stührmann, T., Brüchert, V., Van Der Plas, A., Mohrholz, V., Lam, P., Mußmann, M., Fuchs, B. M., Amann, R., Lass, U. and Kuypers, M. M. M.: Detoxification of sulphidic African shelf waters by blooming chemolithotrophs, Nature, 457(7229), 581–584, doi:10.1038/nature07588, 2009.

67. Lehmann, M. F., Bernasconi, S. M., Barbieri, A., Simona, M. and McKenzie, J. A.: Interannual variation of the isotopic composition of sedimenting organic carbon and nitrogen in Lake Lugano: A long-term sediment trap study, Limnol. Oceanogr., 49, 839-849, doi:10.4319/lo.2004.49.3.0839, 2004.

68. Lehmann, M. F., Sigman, D. M., McCorkle, D. C., Granger, J., Hoffmann, S., Cane, G. and Brunelle, B. G.: The distribution of nitrate $^{15}N/^{14}N$ in marine sediments and the impact of benthic nitrogen loss on the isotopic composition of oceanic nitrate, Geochim. Cosmochim. Acta, 71(22), 5384–5404, doi:10.1016/j.gca.2007.07.025, 2007.

69. Locarnini, R. A., Mishonov, A. V., Antonov, J. I., Boyer, T. P., Garcia, H. E., Baranova, O. K., Zweng, M. M., Paver, C. R., Reagan, J. R., Johnson, D. R., Hamilton, M. and Seidov, D.: World Ocean Atlas 2013. Vol. 1: Temperature, NOAA Atlas NESDIS 73, 40 pp., 2013.

70. Marconi, D., Weigand, M. A., Rafter, P. A., McIlvin, M. R., Forbes, M., Casciotti, K. L. and Sigman, D. M.: Nitrate isotope distributions on the US GEOTRACES North Atlantic cross-basin section: Signals of polar nitrate sources and low latitude nitrogen cycling, Mar. Chem., 177, 143-156, doi:10.1016/j.marchem.2015.06.007, 2015.

71. Marconi, D., Kopf, S., Rafter, P. A. and Sigman, D. M.: Aerobic respiration along isopycnals leads to overestimation of the isotope effect of denitrification in the ocean water column, Geochim. Cosmochim. Ac., 197, 417-432, doi:10.1016/j.gca.2016.10.012, 2017.

72. Mariotti, A.: Atmospheric nitrogen is a reliable standard for natural ^{15}N abundance measurements, Nature, 303(5919), 685–687, doi:10.1038/303685a0, 1983.

73. Mariotti, A., Germon, J. C., Hubert, P., Kaiser, P., Letolle, R., Tardieux, A. and Tardieux, P.: Experimental determination of nitrogen kinetic isotope fractionation: Some principles; illustration for the denitrification and nitrification processes, Plant Soil, 62, 413-430, doi:10.1007/BF02374138, 1981

74. Martin, J. H., Knauer, G. A., Karl, D. M. and Broenkow, W. W.: VERTEX: carbon cycling in the northeast Pacific, Deep-Sea Res., 34, 267-285, doi:10.1016/0198-0149(87)90086-0, 1987.

75. Martin, T. S. and Casciotti, K. L.: Nitrogen and oxygen isotopic fractionation during microbial nitrite reduction, Limnol. Oceanogr., 61, 1134-1143, doi:10.1002/lno.10278, 2016.

76. Martin, T. S. and Casciotti, K. L.: Paired N and O isotopic analysis of nitrate and nitrite in the Arabian Sea oxygen deficient zone, Deep-Sea Res. Pt. I, 121, 121-131, doi:10.1016/j.dsr.2017.01.002, 2017.

77. Monteiro, F. M., Dutkiewicz, S. and Follows, M. J.: Biogeographical controls on the marine nitrogen fixers, Global Biogeochem. Cy., 25, GB2003, doi:10.1029/2010GB003902, 2011.

78. Moore, J. K. and Doney, S. C.: Iron availability limits the ocean nitrogen inventory stabilizing feedbacks between marine denitrification and nitrogen fixation, Global Biogeochem. Cy., 21, GB2001, doi:10.1029/2006GB002762, 2007.

79. Moore, J. K., Doney, S. C. and Lindsay, K.: Upper ocean ecosystem dynamics and iron cycling in a global three-dimensional model, Global Biogeochem. Cy., 18, GB4028, 2004, doi:10.1029/2004GB002220, 2004.

80. Nixon, S. W., Ammerman, J. W., Atkinson, L. P., Berousky, V. M., Billen, G., Boicourt, W. C., Boynton, W. R., Church, T. M., Ditoro, D. M., Elmgren, R., Garber, J. H., Giblin, A. E., Jahnke, R. A., Owens, N. J. P., Pilson, M. E. Q. and Seitzinger, S. P.: The fate of nitrogen and phosphorus at the land-sea margin of the North Atlantic Ocean Five major rivers with an average water flow exceeding 3000 m^3s^{-1} discharge, Biogeochemistry, 35, 141–180, 1996.

81. Noffke, A., Hensen, C., Sommer, S., Scholz, F., Bohlen, L., Mosch, T., Graco, M. and Wallmann, K.: Benthic iron and phosphorus fluxes across the Peruvian oxygen minimum zone, Limnol. Oceanogr., 57(3), 851–867, doi:10.4319/lo.2012.57.3.0851, 2012.

82. Peng, X., Fuchsman, C. A., Jayakumar, A., Warner, M. J., Devol, A. H. and Ward, B. B.: Revisiting nitrification in the Eastern Tropical South Pacific: A focus on controls, J. Geophys. Res.-Oceans, 121, 1667-1684, doi:10.1002/2015JC011455, 2016.

83. Penn, J., Weber, T. and Deutsch, C.: Microbial functional diversity alters the structure and sensitivity of oxygen deficient zones, Geophys. Res. Lett., 43, 9773-9780, doi:10.1002/2016GL070438, 2016.

84. Peters, B. D., Babbin, A. R., Lettmann, K. A., Mordy, C. W., Ulloa, O., Ward, B. B. and Casciotti, K. L.: Vertical modeling of the nitrogen cycle in the eastern tropical South Pacific oxygen deficient zone using high-resolution concentration and isotope measurements, Global Biogeochem. Cy., 30, 1661-1681, doi:10.1002/2016GB005415, 2016.

85. Peters, B. D., Lam, P. J. and Casciotti, K. L.: Nitrogen and oxygen isotope measurements of nitrate along the US GEOTRACES Eastern Pacific Zonal Transect (GP16) yield insights into nitrate supply, remineralization, and water mass transport, Mar. Chem., 201, 137-150, doi:10.1016/j.marchem.2017.09.009, 2018a.

86. Peters, B. D., Horak, R., Devol, A., Fuchsman, C., Forbes, M., Mordy, C. W. and Casciotti, K. L.: Estimating fixed nitrogen loss and associated isotope effects using concentration and isotope measurements of NO_3^-, NO_2^-, and N_2 from the Eastern Tropical South Pacific oxygen deficient zone, Deep-Sea Res. Pt. II, doi:10.1016/j.dsr2.2018.02.011, 2018b.

87. Rafter, P. A. and Sigman, D. M.: Spatial distribution and temporal variation of nitrate nitrogen and oxygen isotopes in the upper equatorial Pacific Ocean, Limnol. Oceanogr., 61, 14-31, doi:10.1002/lno.10152, 2016.

88. Rafter, P. A., DiFiore, P. J. and Sigman, D. M.: Coupled nitrate nitrogen and oxygen isotopes and organic matter remineralization in the Southern and Pacific Oceans, J. Geophys. Res. Oceans, 118, 4781-4794, doi:10.1002/jgrc.20316, 2013.

89. Raimbault, P., Garcia, N. and Cerutti, F.: Distribution of inorganic and organic nutrients in the South Pacific Ocean: evidence for long-term accumulation of organic matter in nitrogen-depleted waters, Biogeosciences, 5, 281-298, doi:10.5194/bg-5-281-2008, 2008.

90. Redfield, A. C., Ketchum, B. H. and Richards, F. A.: The Influence of Organisms on the Composition of Sea Water, Sea, 2, 26-77, 1963.

91. Ryabenko, E., Kock, A., Bange, H. W., Altabet, M. A. and Wallace, D. W. R.: Contrasting biogeochemistry of nitrogen in the Atlantic and Pacific Oxygen Minimum Zones, Biogeosciences, 9, 203-215, doi:10.5194/bg-9-203-2012, 2012.

92. Seitzinger, S. P. and Giblin, A. E.: Estimating denitrification in North Atlantic continental shelf sediments, Biogeochemistry, 35(1), 235–260, doi:10.1007/BF02179829, 1996.

93. Shiozaki, T., Bombar, D., Riemann, L., Hashihama, F., Takeda, S., Yamaguchi, T., Ehama, M., Hamasaki, K. and Furuya, K.: Basin scale variability of active diazotrophs and nitrogen fixation in the North Pacific, from the tropics to the subarctic Bering Sea, Global Biogeochem. Cycles, 31(6), 996–1009, doi:10.1002/2017GB005681, 2017.

94. Sigman, D. M., Altabet, M. A., McCorkle, D. C., Francois, R. and Fischer, G.: The $\delta^{15}N$ of nitrate in the Southern Ocean: Consumption of nitrate in surface waters, Global Biogeochem. Cy., 13, 1149-1166, doi:10.1029/1999GB900038, 1999.

95. Sigman, D. M., Granger, J., DiFiore, P. J., Lehmann, M. F., Ho, R., Cane, G. and van Geen, A.: Coupled nitrogen and oxygen isotope measurements of nitrate along the eastern North Pacific margin, Global Biogeochem. Cy., 19, GB4022, doi:10.1029/2005GB002458, 2005.

96. Sigman, D. M., DiFiore, P. J., Hain, M. P., Deutsch, C., Wang, Y., Karl, D. M., Knapp, A. N., Lehmann, M. F. and Pantoja, S.: The dual isotopes of deep nitrate as a constraint on the cycle and budget of oceanic fixed nitrogen, Deep-Sea Res. Pt. I, 56, 1419-1439, doi:10.1016/j.dsr.2009.04.007, 2009.

97. Somes, C. J., Schmittner, A., Galbraith, E. D., Lehmann, M. F., Altabet, M. A., Montoya, J. P., Letelier, R. M., Mix, A. C., Bourbonnais, A. and Eby, M.: Simulating the global distribution of nitrogen isotopes in the ocean, Global Biogeochem. Cy., 24, GB4019, doi:10.1029/2009GB003767, 2010.

98. Somes, C. J. and Oschlies, A.: On the influence of "non-Redfield" dissolved organic nutrient dynamics on the spatial distribution of N_2 fixation and the size of the marine fixed nitrogen inventory, Global Biogeochem. Cycles, 29(7), 973–993, doi:10.1002/2014GB005050, 2015.

99. Strous, M., Fuerst, J. A., Kramer, E. H. M., Logemann, S., Muyzer, G., van de Pas-Schoonen, K. T., Webb, R., Kuenen, J. G. and Jetten, M. S. M.: Missing lithotroph identified as new planctomycete, Nature, 400, 446-449, doi:10.1038/22749, 1999

100. Van Mooy, B. A. S., Keil, R. G. and Devol, A. H.: Impact of suboxia on sinking particulate organic carbon: Enhanced carbon flux and preferential degradation of amino acids via denitrification, Geochim. Cosmochim. Ac., 66, 457-465, doi:10.1016/S0016-7037(01)00787-6, 2002.

101. Ward, B. B.: How Nitrogen Is Lost, Science, 341(6144), 352–353, doi:10.1126/science.1240314, 2013.

102. Westberry, T., Behrenfeld, M. J., Siegel, D. A. and Boss, E.: Carbon-based primary productivity modeling with vertically resolved photoacclimation, Global Biogeochem. Cy., 22, GB2024, doi:10.1029/2007GB003078, 2008.
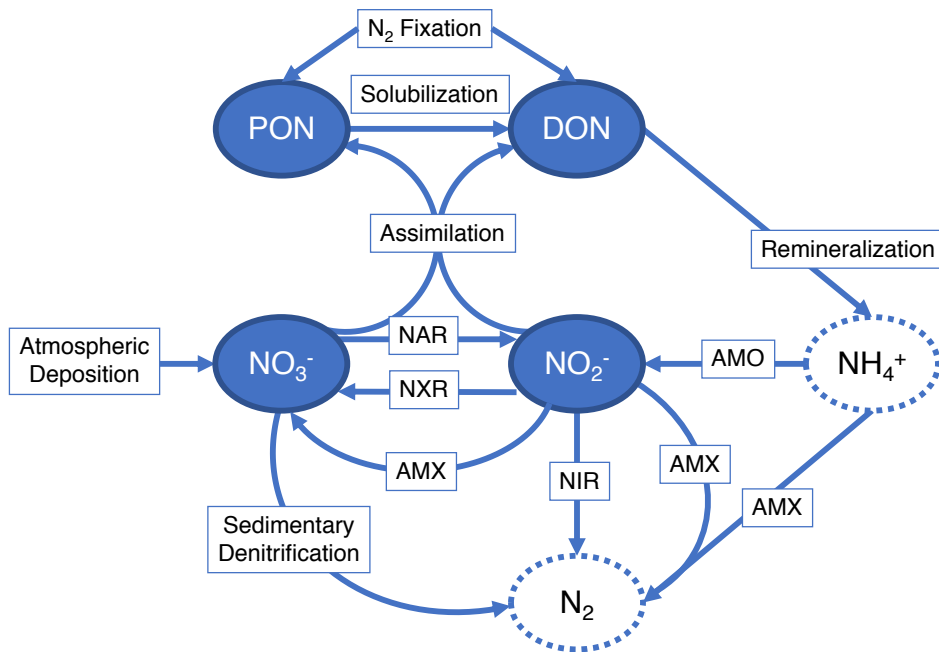
Figure 1: Diagram showing the nitrogen (N) cycle processes represented in the model. Two organic N pools are modeled: particulate organic N (PON) and dissolved organic N (DON). Two inorganic N pools are modeled: nitrate (NO_3^-) and nitrite (NO_2^-). N source processes are nitrogen (N_2) fixation and atmospheric deposition. N sink processes are sedimentary denitrification, NO_2^- reduction (NIR), and anammox (AMX). Internal cycling processes that transform N from one species to another are solubilization, remineralization, assimilation, NO_3^- reduction (NAR), ammonia oxidation (AMO), and NO_2^- oxidation (NXR). Neither ammonia (NH_3) nor ammonium (NH_4^+) are tracked in this model, since they are assumed to not accumulate. N_2 is also not explicitly accounted for in the model.
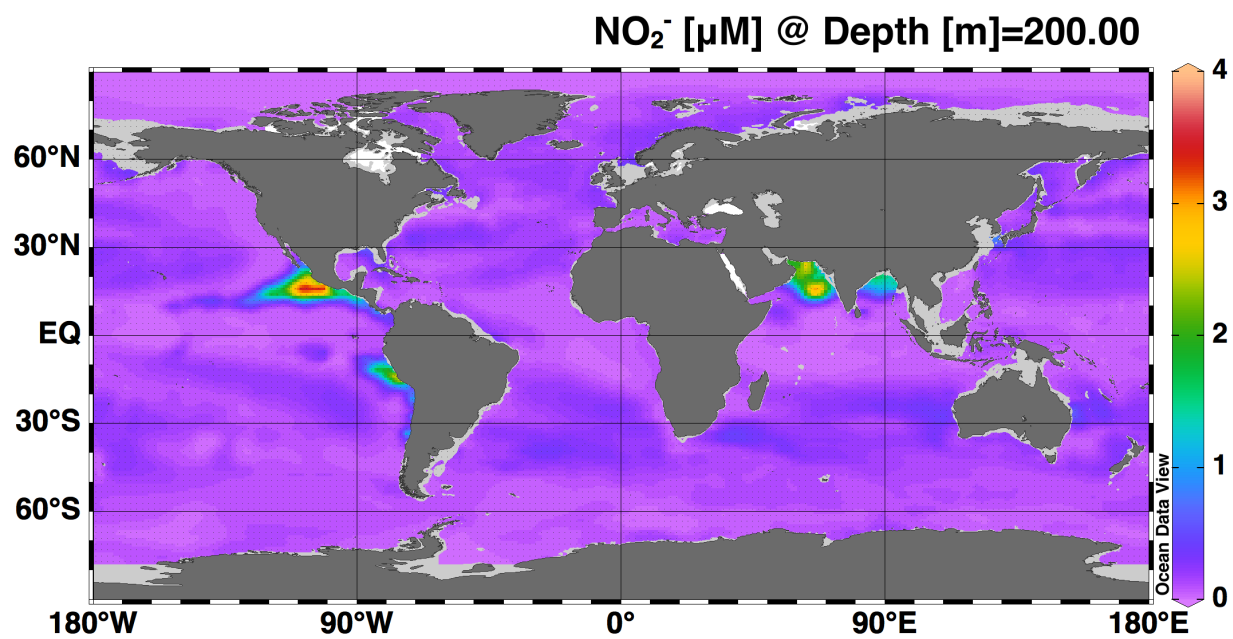
Figure 2: Map showing the model-estimated accumulation of nitrite (NO₂⁻) at 200 m depth.
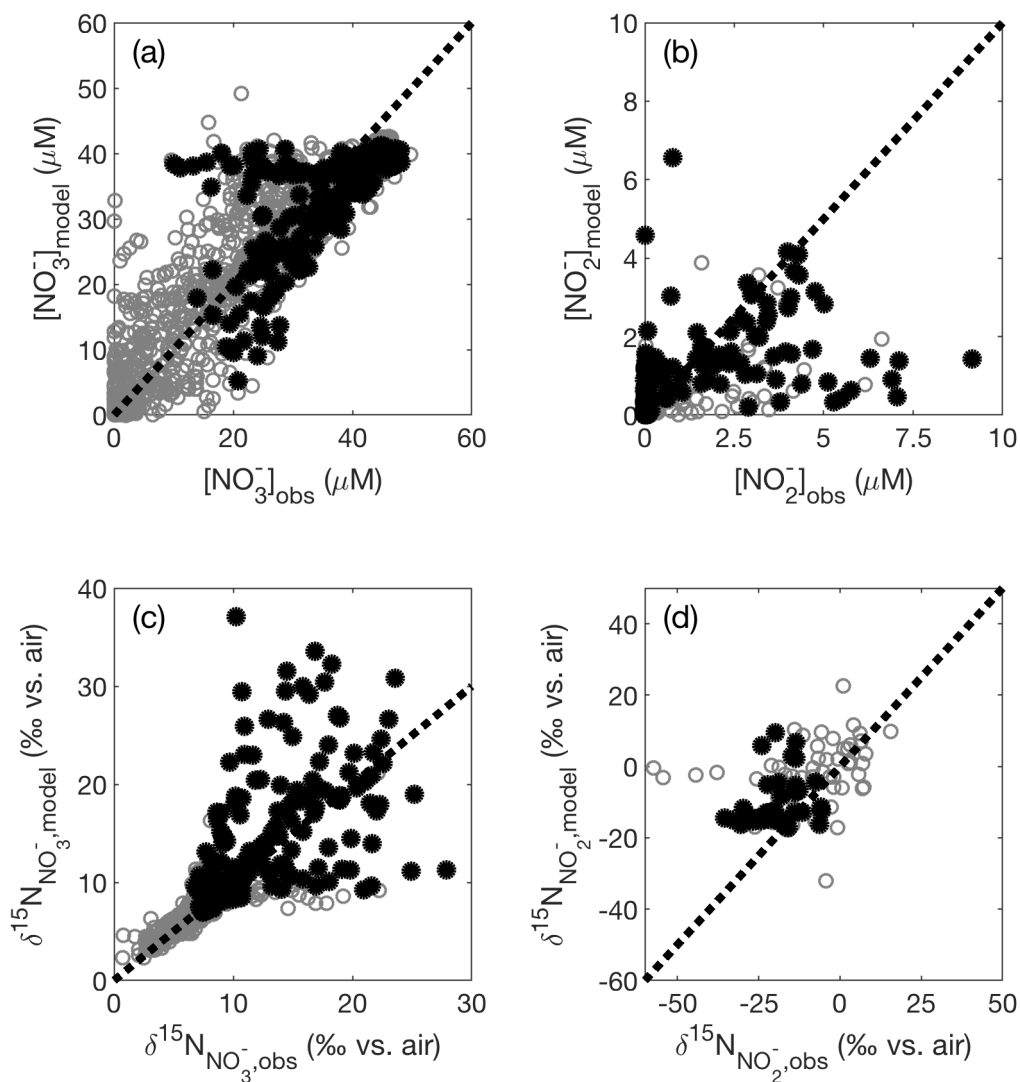
Figure 3: Modeled (a) [NO₃⁻], (b) [NO₂⁻], (c) δ¹⁵N_NO3, and (d) δ¹⁵N_NO2 are compared against the corresponding values from the database test set. Shown on each panel is a 1:1 line starting at the origin. Data in black have corresponding [O₂] < 10 μM, and data in gray have [O₂] ≥ 10 μM.
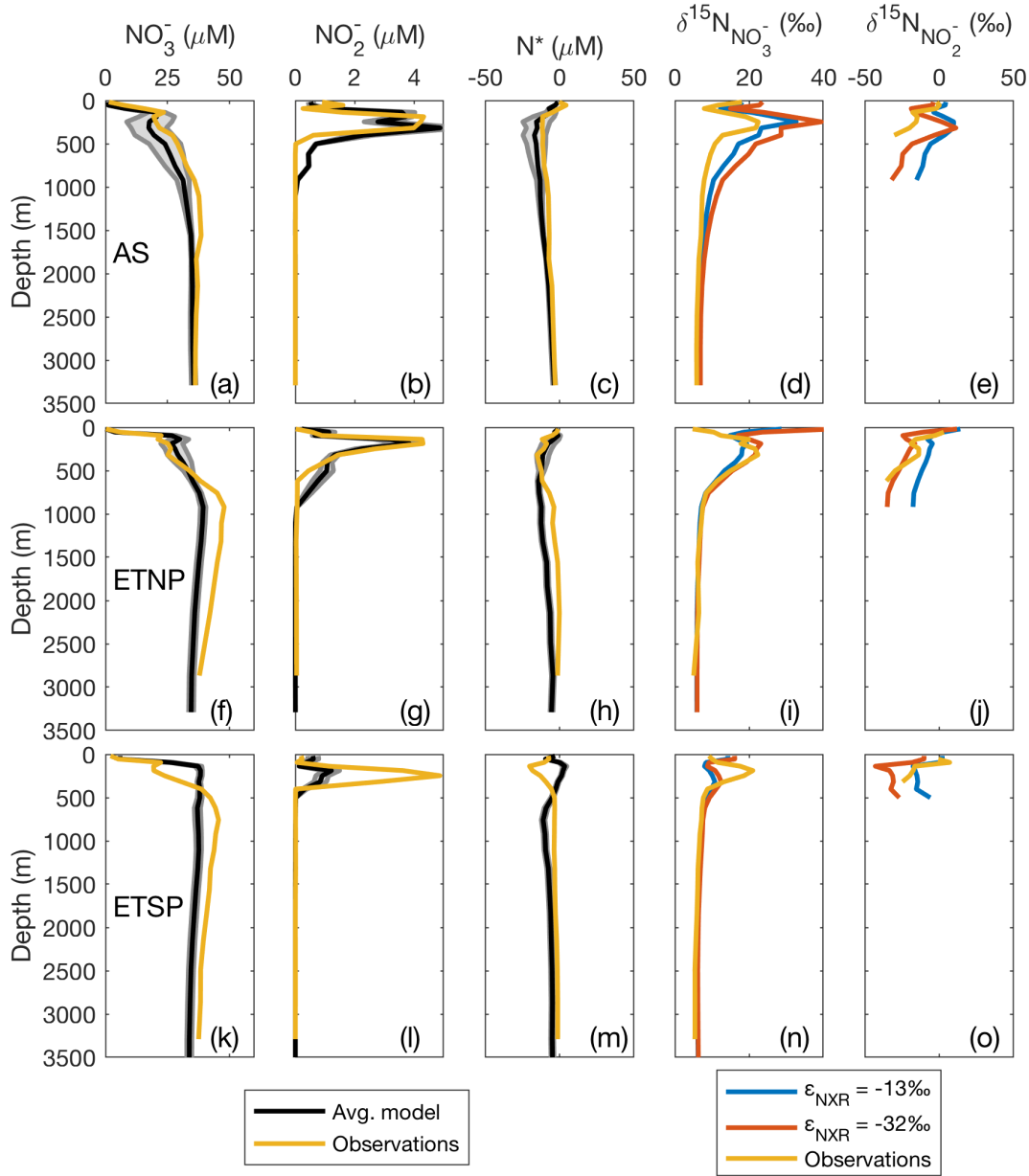
Figure 4: Offshore depth profiles comparing model results with binned and averaged database observations from a model water column. Results are shown for the three main oxygen deficient zones (ODZs): the Arabian Sea (a-e), the Eastern Tropical North Pacific (ETNP; f-j), and the Eastern Tropical South Pacific (ETSP; k-o). Average modeled nitrate concentration ([NO₃]), nitrite concentration ([NO₂]), and N* are shown in black. Gray error lines around the black line show the 2σ spread from the average from the 12 different optimized model results using the different combinations of isotope effects for nitrate reduction (ε$_{NAR}$), nitrite reduction (ε$_{NIR}$), and nitrite oxidation (ε$_{NXR}$). Observed data are shown in yellow in all panels. Modeled δ^{15}N$_{NO3}$ and δ^{15}N$_{NO2}$ are shown for three different combinations of isotope effect. The blue lines represent ε$_{NAR}$ = 13, ε$_{NXR}$ = -13, and ε$_{NIR}$ = 0, which are the best fit isotope effects globally and in the ETSP. The red lines represent ε$_{NAR}$ = 13, ε$_{NXR}$ = -32, and ε$_{NIR}$ = 0, which are the best fit isotope effects in the Arabian Sea.
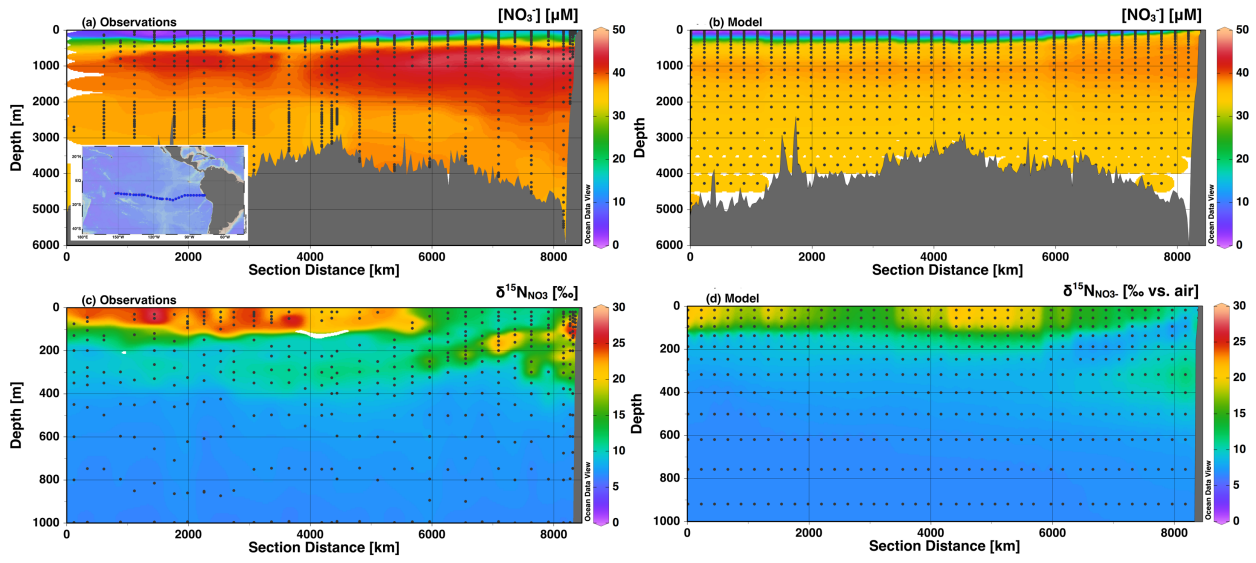
Figure 5: Section profiles of NO₃⁻ concentrations and isotopes over the GP16 cruise track (panel (a) inset) in the South Pacific. Profiles are presented from east (right) to west (left). Comparison of (a) observed [NO₃⁻] to (b) modeled [NO₃⁻] is presented over the full depth range (0-6000m). Comparison of (c) observed δ¹⁵N_{NO3} to (d) modeled δ¹⁵N_{NO3} is presented over a shortened depth range (0-1000m) to better assess surface and ODZ values. GEOTRACES data are from Peters et al. (2018a) and available from BCO-DMO.
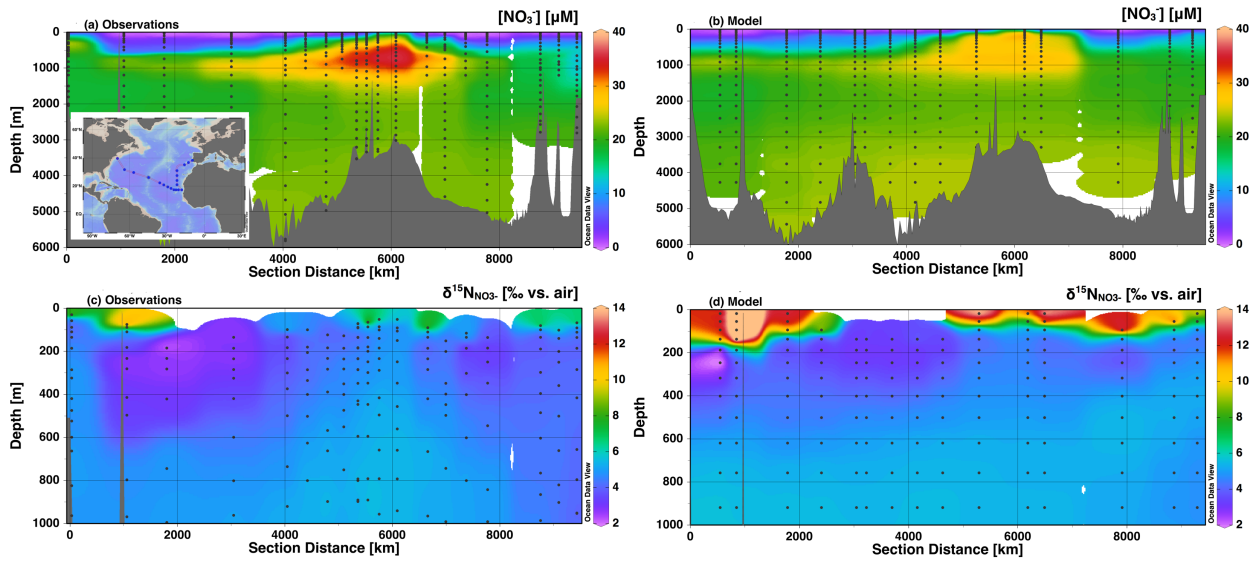
Figure 6: Section profiles of NO$_3^-$ concentrations and isotopes over the GA03 cruise track (panel (a) inset) in the North Atlantic. Profiles are presented from east (right) to west (left) from 0-6000km section distance, and then from south to north. Comparison of (a) observed [NO$_3^-$] to (b) modeled [NO$_3^-$] is presented over the full depth range (0-6000m). Comparison of (c) observed δ^{15}N$_{NO3}$ to (d) modeled δ^{15}N$_{NO3}$ is presented over a shortened depth range (0-1000m) to better assess surface and the low δ^{15}N$_{NO3}$ contribution from N$_2$ fixation. GEOTRACES data are from Marconi et al. (2015) and available from BCO-DMO.
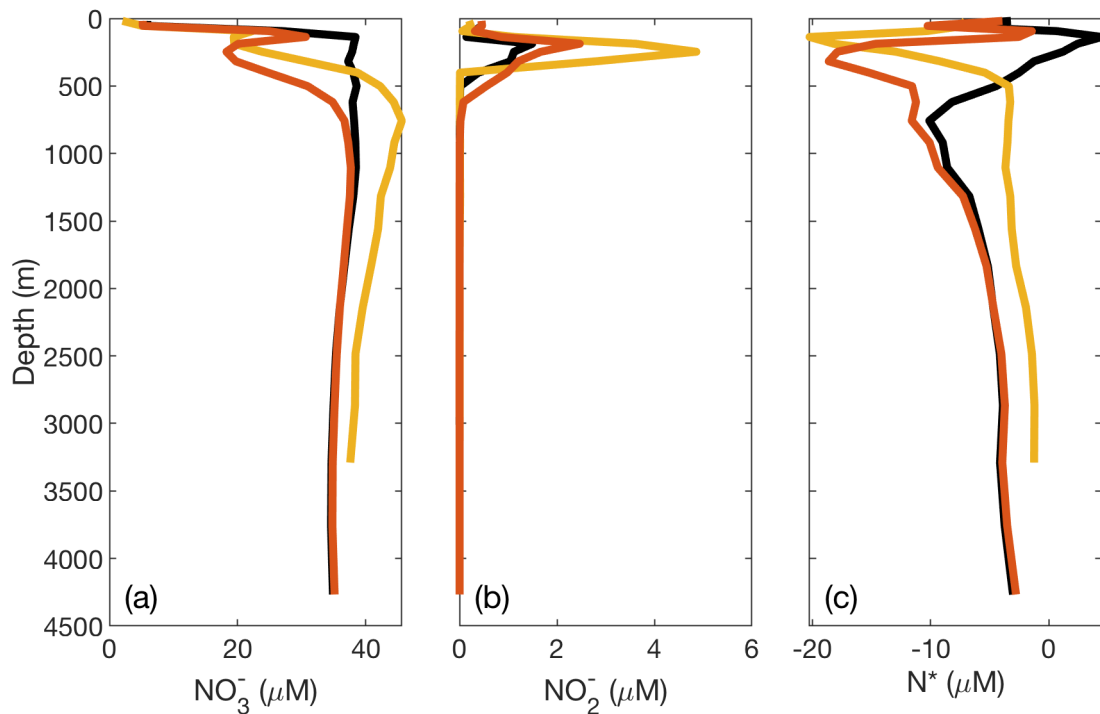
Figure 7: Plot of DIN concentrations and N* from the ETSP ODZ comparing modified O₂ thresholds for N loss. In the original optimized version of the model, there is insufficient N loss and NO₂⁻ accumulation in the ETSP. To demonstrate that this issue may be caused by issues with the gridded averages of O₂ and model grid size in the ETSP, we raised the O₂ thresholds for N loss-related processes (NAR, NIR, and AMX) to 15 μM. This effectively lowers the observed [O₂] in order to stimulate N loss. The resulting (a) [NO₃⁻], (b) [NO₂⁻], and (c) N* are shown with the observed values from the database (yellow), original optimized model values (black), and lowered O₂ threshold model values (red).

Parameter	Value	Reference
b	-0.858	Martin et al., 1987
F_0	1.5 mmol N m^{-3} yr^{-1}	DeVries et al., 2013 Capone et al., 2005
λ	10 mmol N m^{-3}	Holl & Montoya, 2005
T_0	20 ˚C	DeVries et al., 2013 Capone et al., 2005
K_{Fe}	4.4*10^{-5} mmol Fe m^{-3}	Follows et al., 2007
K_P	0.005 mmol PO$_4^{3-}$ m^{-3}	Moore & Doney, 2007
$r_{C:N}$	6.625	Redfield et al., 1963
K_m^{AMO}	3.5 µM O$_2$	Peng et al., 2016
K_m^{NXR}	0.8 µM O$_2$	Bristow et al., 2016b
O_2^{NAR}	7 µM O$_2$ 15 µM O$_2$[a]	Dalsgaard et al., 2014; Jensen et al., 2008; Kuypers et al., 2005; Kalvelage et al., 2011
O_2^{NIR}	5 µM O$_2$ 15 µM O$_2$[a]	Bonin et al., 1989; Kalvelage et al., 2011
O_2^{AMX}	10 µM O$_2$ 15 µM O$_2$[a]	Dalsgaard et al., 2014; Jensen et al., 2008; Kuypers et al., 2005; Kalvelage et al., 2011
$\delta^{15}N_{dep}$	-4‰	Hastings et al., 2009
$\delta^{15}N_{fix}$	-1‰	Hoering & Ford, 1960; Carpenter et al., 1997
$\alpha_{AMX,NO2}$	1.016	Brunner et al., 2013
$\alpha_{AMX,NXR}$	0.969	Brunner et al., 2013
$\alpha_{AMX,NH4}$	1	
α_{AMO}	1	
α_{sed}	1	Brandes & Devol, 1997; Lehmann et al., 2004
α_{assim}	1.004	Granger et al., 2010
α_{remin}	1	Casciotti et al., 2008; Möbius, 2013
α_{sol}	1	Knapp et al., 2011

a. Value used in test of ETSP N loss issue (Section 4.2)

Table 1. Non-optimized model parameters.

Parameter	Initial	Final (avg.)	Error (2σ)	Final (global best fit)
$^{14}k_{PON}$ (yr^{-1})	3.9	3.9	0	3.9
$^{14}k_{DON}$ (yr^{-1})	1.8	0.8	0.2	0.6
$^{14}k_{NXR}$ (yr^{-1})	6.0	16.0	3.0	18.7
$^{14}k_{NAR}$ (μM^{-1} DON)	2.5	1.6	0.8	2.3
$^{14}k_{NIR}$ (μM^{-1} DON)	1.5	1.7	1.0	2.6

Table 2. Optimized model parameters.

Parameter	Values	References
ε_{NAR}	13‰, 25‰	Granger et al., 2008
		Kritee et al., 2012
		Casciotti et al., 2013
		Marconi et al., 2017
ε_{NIR}	0‰, 15‰	Casciotti et al., 2013
		Martin and Casciotti, 2016
ε_{NXR}	-32‰, -20‰, -13‰	Casciotti, 2009
		Buchwald and Casciotti, 2010
		Casciotti et al., 2013

Table 3: Isotope effect cases.